ACS OMEGA

Open Access

This article is licensed under CC-BY-NC-ND 4.0

http://pubs.acs.org/journal/acsodf

Article

XPS Investigation of Co−Ni Oxidized Compounds Surface Using Peak-On-Satellite Ratio. Application to $Co_{20}Ni_{80}$ Passive Layer Structure and Composition

Barbara Laïk,* Morgane Richet, Nicolas Emery, Stephane Bach, Loïc Perrière, Yvan Cotrebil, Vincent Russier, Ivan Guillot, and Pierre Dubot

Cite This: *ACS Omega* 2024, 9, 40707−40722

Read Online

ACCESS | Metrics & More | Article Recommendations | Supporting Information

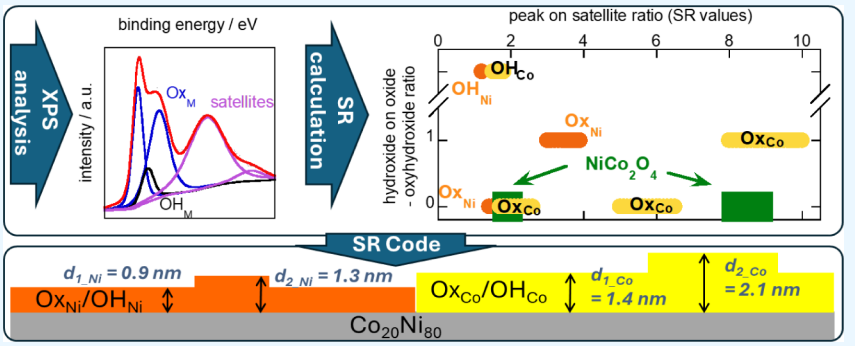

ABSTRACT: XPS data processing for cobalt and nickel core-level peaks can be complicated. This is especially true when analyzing a mixture of oxide/oxyhydroxide/hydroxide compounds of these metals. The objective of this study is to develop a method for decomposing XPS spectra of 2p core levels for nickel and cobalt-oxidized compounds. This methodology was then employed to study the passivation layer of the $Co_{20}Ni_{80}$ alloy. The analysis of Ni_{2p} and Co_{2p} photo peaks using a homemade code based on core-level peak structure and satellites enables us to determine the chemical composition of the surface layer, knowledge of which is particularly important because it is directly linked to the anticorrosive properties it confers on the surface of the oxidized alloy. The XPS analysis, coupled with sequential ion sputtering, revealed that the passive layer of the $Co_{20}Ni_{80}$ alloy is heterogeneously covered with either oxidized cobalt compounds or oxidized nickel compounds. The method used also demonstrates that the chemical heterogeneity is associated with the thickness heterogeneity of the passive layer.

INTRODUCTION

Due to their interesting chemical and physical properties, nickel, cobalt, and their alloys offer a wide range of applications. For example, research in the low-carbon production of hydrogen as part of the energy transition is largely focused on the use of such alloys as electrode materials. With low hydrogen overpotential, they have very good electrocatalytic activity for water electrolysis in alkaline media.[1−3] Ni−Co alloys are also widely used in the design of materials with magnetic properties, such as microsensors, accumulators, and inductors.[4,5] Their high hardness, wear resistance, and corrosion resistance are of interest to the automotive and aerospace industries. They could be an alternative to hard chromium.[6] For many applications, the alloy is used in the form of thin films that can be prepared by different techniques, e.g., sputtering,[7−9] chemical vapor deposition, or electrochemical deposition.[10−18]

The electronic structure of the surface layer, and more specifically, the semiconducting property of oxidized Co and Ni compounds, is related to their anticorrosive properties. In fact, it is the structure and composition of the passive films spontaneously formed on the alloy surface that give the material its corrosion resistance.[19−23] For this reason, particular attention must be paid to the passive layer structure and composition of these alloys, which are of great interest in the aerospace sector. In this context, by comparing two alloys of the same composition, but produced by either melting or electroforming, Dorenlor's work focused on establishing a relationship between microstructural parameters and corrosion resistance.[24] In order to correlate the microstructure of the $Co_{20}Ni_{80}$ alloy with the anticorrosive properties of the passivation layer, it seems obvious to first study the

Received: May 30, 2024
Revised: September 2, 2024
Accepted: September 5, 2024
Published: September 18, 2024

ACS Publications

© 2024 The Authors. Published by American Chemical Society

composition and structure of the layer formed naturally or electrochemically on the surface of the alloy. Both the in-depth chemical composition and the topological structure of thin films can be investigated by X-ray photoemission (XPS) coupled with sequential low-energy ion sputtering (depth profiling), thanks to the modeling of the XPS spectra at each step of the depth profile measurement.

In the first part, we studied some "reference" compounds (CoO, Co_3O_4, $Co(OH)_2$, NiO, $Ni(OH)_2$, and $NiCo_2O_4$) that may be present in the $Co_{20}Ni_{80}$ alloy passivation layer. XPS spectra are discussed in light of the most important characteristic XPS emission peaks of the cobalt and nickel 2p levels that are described in detail in the literature. As the many studies referred to in this section show, it is extremely difficult to determine the chemical composition of a mixture of compounds from the structure of the core-level peaks alone. We have therefore developed a method that combines the analysis of the spectral structure of these levels with the intensity of the satellite peaks that appear in the region.

In a second part, the methodology based on the intensity of the core-level peak-to-satellite ratio to deduce the chemical composition of the surface layer is presented. In the case of the $Co_{20}Ni_{80}$ alloy, the evolution of the in-depth chemical composition can be determined. In the case of "reference" compounds, it is possible to determine a surface composition that is different from that of the bulk.

In the last part, a second modeling of the evolution of the XPS spectra with sputtering time allows not only the determination of the in-depth distribution of the chemical compounds but also the estimation of the different thicknesses and coverings of the compounds that form a heterogeneous passive layer (chemically and topologically).

MATERIALS AND METHODS

The $Co_{20}Ni_{80}$ alloy was prepared by mixing small chips of Co and Ni metals with a purity of more than 99.95% by weight. Raw metals are melted by high-frequency electromagnetic induction in a water-cooled copper crucible under He atmosphere. Then gravity casting was performed to shape an ingot with a diameter of 12.7 mm, a length of around 60 mm, and an estimated cooling rate of around 10^3 K·s^{-1}. The rod was cut into slices of around 2−3 mm in length, then cut in half. Samples were finally prepared by mechanical grinding using 1200−4000 SiC papers. The samples were characterized by X-ray diffraction (XRD) with a PANalytical X'Pert Pro diffractometer using the Co Kα radiation at a wavelength of 0.178897 nm.

XRD patterns of pure oxides or hydroxides of cobalt and nickel were analyzed using the Bruker DIFFRAC.TOPAS v7 software[25] using the Rietveld method for $Co(OH)_2$, Co_3O_4, and $NiCo_2O_4$ or the Pawley method for CoO(OH) and $Ni(OH)_2$. Since several phases are highly textured due to their lamellar structure, the generalized geometric approach to figure out the anisotropic peak broadening developed by Ectors et al. has been used.[26]

The $Co(OH)_2$ has been prepared by dissolving $Co(NO_3)_2{\cdot}6H_2O$ in a deionized water/ethanol mixture (50/50 in volume). NaOH was added in excess to the solution and continuously stirred until the formation of a precipitate. The product powder was then filtered and washed several times with water and ethanol to remove the excess sodium hydroxide. The sample was dried in an oven at 120 °C overnight. The XRD pattern (Figure S.I.1) is easily indexed with the hexagonal structure of $Co(OH)_2$. The related cell parameters, a = 0.3180 (1) nm and c = 0.4657 (2) nm, are in good agreement with those reported in the literature.[27] However, small traces of CoO(OH) were detected in the XRD pattern. CoO(OH) was formed in a two-step reaction. The first step, as for the synthesis of $Co(OH)_2$, involves the dissolution of $Co(NO_3)_2{\cdot}6H_2O$ in a mixture of deionized water and ethanol (50/50 in volume) and the addition of NaOH in excess. Second, H_2O_2 solution (30%) was added in excess dropwise to the $Co(OH)_2$ suspension under continuous stirring to form CoO(OH) by oxidation of Co^{2+} in Co^{3+}. The brown precipitate was then filtered and washed several times with water and ethanol. The XRD pattern (Figure S.I.2) is well fitted using the rhombohedral structure proposed by Delaplane et al.[28] The obtained cell parameters a = 0.2854 (1) nm and c = 1.3205 (3) nm are consistent with those of the literature. Co_3O_4 was obtained by thermal decomposition at 350 °C of the $Co(OH)_2$ powder prepared above. The XRD pattern (Figure S.I.3) was easily fitted with a spinel structure of cell parameter a = 0.8081 (2) nm, in line with the previous report.[29]

The $Ni(OH)_2$ was prepared, in a similar way to cobalt hydroxide, from $Ni(NO_3)_2{\cdot}6H_2O$ dissolved in a deionized water/ethanol mixture (50/50 in volume). NaOH was added in excess to precipitate $Ni(OH)_2$. The product was washed several times with water and ethanol and then dried at 120 °C. The obtained diffraction pattern, which exhibits broad and ill-defined peaks, has been fitted with a hexagonal lamellar structure with a = 0.312 (1) nm and c = 0.481 (6) nm (Figure S.I.4). $NiCo_2O_4$ was prepared from $Co(NO_3)_2{\cdot}6H_2O$ and $Ni(NO_3)_2{\cdot}6H_2O$ dissolved in a stoichiometric ratio in deionized water. Oxalic acid was added to the solution as a complexing agent in stoichiometric proportion with regard to the metallic cation proportion. The obtained precipitate was washed several times with deionized water, dried in an oven at 120 °C, and then heated to 300 °C to prepare the phase. The diffraction pattern (Figure S.I.5) has been fitted with a single spinel phase of cell parameter a = 0.8122 (6) nm, in agreement with literature data.[30] Commercial NiO (R.P. Normapur for analysis—Prolabo) and CoO (Sigma-Aldrich—CAS 1307-96-6) were used as reference.

Surface analysis was achieved by combining X-ray photoelectron spectroscopy (XPS) and sequential Ar^+ ion sputtering. XPS analysis was performed using a Thermo Electron Kalpha spectrometer, with a monochromatic Al Kα X-ray source ($h\nu$ = 1486.6 eV) operating at a pressure of around 10^{-9} mbar. The analyzer pass energy was 200 eV for survey spectra and 50 eV for high-resolution spectra. The spectrometer was calibrated using Au $4f_{7/2}$ at 84.1 eV, and when necessary, the energy scale was corrected by reference to the C_{1s} of aliphatic compounds at 285.0 eV. Photoelectrons are collected perpendicularly from the sample surface, so the cosine factor appearing in the photoelectron intensity exponential attenuation law is set to 1. To avoid significant spectral modifications of the 2p region observed and related to irradiation damages (ion beam-induced reduction, preferential sputtering, and energy-induced phase transformation), the ion sputtering was carried out with low-energy argon ions (200 eV). The ion gun (Thermo EX06) allows it to work with such low primary energy. Under these conditions, spectral evolutions between two etching steps are due to material removal without other induced chemical modifications. The surface density of ions used was the lowest possible and corresponds approximately to less than 1 μA for a

https://doi.org/10.1021/acsomega.4c05082
ACS Omega 2024, 9, 40707−40722

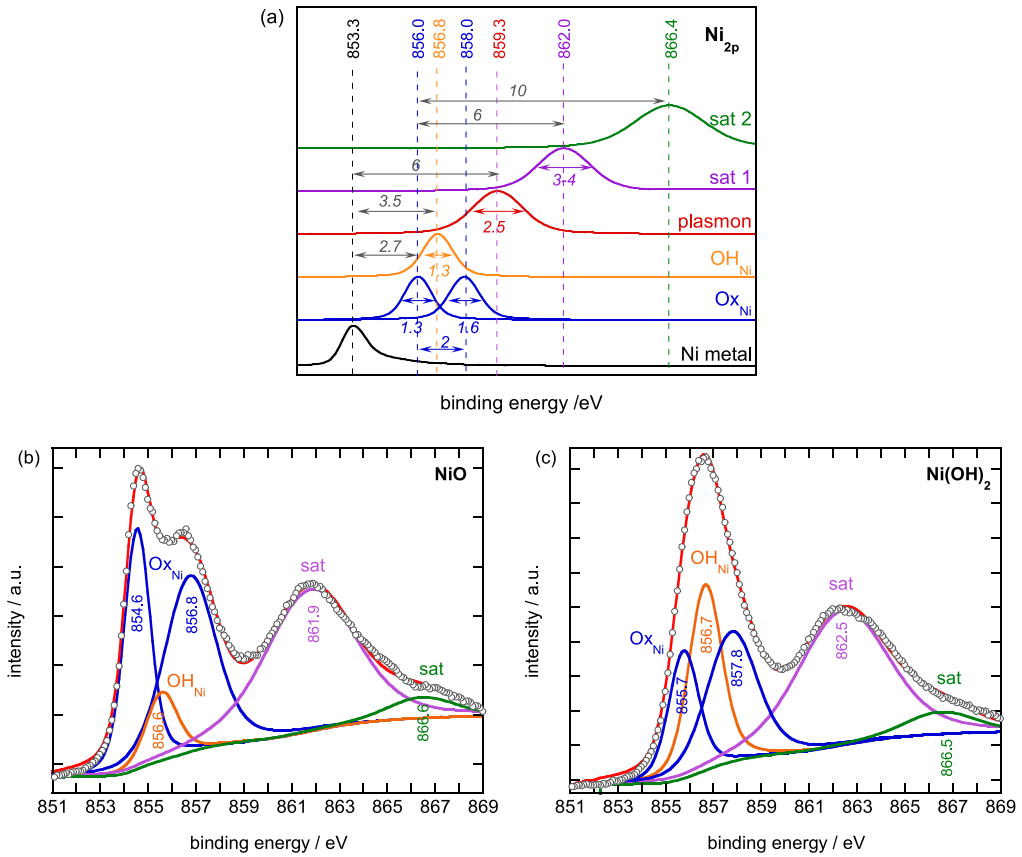

Figure 1. (a) Schematic representation of the different components describing the Ni_{2p} spectral fingerprint (extracted values from literature) and experimental spectra of (b) NiO and (c) $Ni(OH)_2$ fitted with the different spectral contributions.

swept surface of about 3 × 2 mm^2. This gives a sputtering speed of ca. 0.06 nm s^{-1} on the Thermo Electron Ta_2O_5 scale. Of course, the sputtering speed on the considered samples in this work should be slightly different, but it gives a good estimation of it. For in-depth analysis, 14 sputtering steps of 2 s were performed, i.e., 28 s of total ion sputtering, resulting in an analyzed thin film depth of approximately 2 nm.

Spectra were recorded and analyzed using Thermo Avantage software. A Shirley-type background subtraction was performed prior to peak fitting. Nonmetallic peaks (oxides, hydroxides) were modeled with a fixed 30/70% Lorentzian/Gaussian peak shape. Peaks corresponding to the metallic state have been modeled with an asymmetric peak mimicking the shape of the Doniach-Sunjic line. The asymmetric line shape modeling depends on three parameters: tail mix, tail height, and tail exponent. In the peak fitting process, these three parameters were set, respectively, to 50.0, 0.0, and 0.06, and were allowed to vary in a range of 5% from these values. During the fitting process, i.e., when adjusting the various contributions to reproduce the total experimental spectrum as closely as possible, the energy and full width at half-maximum of all peaks were constrained to vary within a small range (±0.15 eV) of the reference spectra values.

RESULTS

XPS Analysis of the Ni_{2p} and Co_{2p} Core Levels. Introduction to the Peak-On-Satellite Ratio. XPS has been extensively used in the literature to study the surface chemistry and electronic structure of Ni and Co compounds. Many studies have focused on the nature of the satellite structures that appear on the high binding energy side of the core-level photopeaks, which are thought to arise from multielectron excitations (shakeup) and/or configuration interactions.[31,32] Other studies focused on the multiplet structure of the localized 3d-level in tetrahedral or octahedral local environments (anions in oxides), which split into e_g and t_{2g} bands.[31,33,34] These are just a few cited references to highlight the complexity of spectroscopic interpretations of surfaces containing both cobalt and nickel oxidized compounds from their 2p photoelectron spectra.

In the case of passivation layers, the system is even more complex, as the initial preparation of the metal surface under investigation can affect the adsorbed species and surface reactive sites that lead to the oxidized compounds. Differences in preparation may therefore result in different surface layer compositions or structures. It is quite common to detect different oxidation states, crystallographic structures, and chemical compounds in many XPS studies reported on oxide layers grown on a metal surface in a humid atmosphere at room temperature.[35,36] It should be noted that in the case of alloys, the interpretation of the spectra can be much more complex due to a wider range of possible chemical compounds being distributed either in the depth of the film or laterally in the oxide thin film.

Despite these inherent difficulties arising from the physical processes leading to spectral complexity, some articles by Biesinger, Grosvenor, McIntyre,[37−40] Yang,[41] Gonzalez-Elipe,[42] and Weidler[43] describe the possibility of assigning a 2p spectral fingerprint for pure nickel and/or cobalt oxides and hydroxylated compounds. The spectral identification and

https://doi.org/10.1021/acsomega.4c05082
ACS Omega 2024, 9, 40707−40722

Table 1. Satellite Ratio (SR) Values Reported in Literature for the Different Considered Oxides/Oxyhydroxides/Hydroxides of Cobalt or Nickel and for the $NiCo_2O_4$ Spinel

Cobalt			Nickel		
Compound *i*	SR_i	Ref	Compound *i*	SR_i	Ref
CoO	1.7−2.6	40,51,52	NiO	1.5 ±0.1	39,40
Co_3O_4	5.0−6.5	40,41,51,52	Ni_2O_3	1.4	57,58
$NiCo_2O_4$	8.0−9.0	53−55	$NiCo_2O_4$	1.9 ± 0.1	53−55
CoO(OH)	8.0−10.0	40,41,56	$\gamma-\beta$ NiO(OH)	3.0−4.0	39,59−61
$Co(OH)_2$	1.5−1.8	40,41	$Ni(OH)_2$	1.2 ± 0.1	39,41

multiplet decomposition used in this paper are based on these works.

Nickel Compounds. A schematic representation of the different components taken from the literature describing Ni_{2p} spectra is shown in Figure 1a. The lowest binding energy peak located at 853.3 eV corresponds to the nickel metallic state (Ni^0) and can be modeled by an asymmetric line shape. In the case of pure NiO (Ni^{2+}), the experimental $2p_{3/2}$ peak can be modeled with a simplified fingerprint consisting of only two peaks with different binding energies separated by 2.0 ± 0.15 eV. The lowest-energy one is located at ≃856.0 eV, i.e., at 2.6 ± 0.15 eV from the metal Ni^0 peak, and presents a full width at half maximum (fwhm) of ca. 1.3 ± 0.15 eV. The second is located at around 858.0 eV and has a larger fwhm of about 1.6 ± 0.15 eV (Figure 1a). The origin of this doublet structure is not clear. Some authors attribute the largest peak to an electronic transition in an empty 3d state, in agreement with the optical absorption data,[36,44] while others believe it is linked to the presence of surface defects created after heat treatments of NiO samples that lead to surface dehydroxylation.[45]

In the case of hydroxides and oxyhydroxides ($Ni(OH)_2$, NiO(OH)), the envelope of the multiplet structure proposed by Grosvenor et al.[38] can be reproduced successfully by a single peak. This experimental peak is located at ≃857.0 eV, i.e., 3.4 ± 0.15 eV higher than the Ni^0 $2p_{3/2}$ peak (Figure 1(a)). This binding energy is intermediate between those of the components of the doublet Ni^{2+} spectrum of NiO described above. Studies by Lobinsky[46] confirm this similar single-peak structure for the Ni_{2p} spectrum of both $Ni(OH)_2$ and NiO(OH). Although these two hydroxylated compounds have very similar 2p spectra, differentiation can be achieved thanks to the two very large satellite peaks (fwhm of 3−4 eV) which are located at higher energy than the main core-level peaks (Figure 1a). They have high intensity for $Ni(OH)_2$ and low intensity for NiO(OH). It is generally accepted that the satellite peak located at ≈862 eV results from an interaction configuration effect due to a strong hybridization between the localized 3d states and the O_{2p} valence orbitals.[45] Tomellini explains that the nickel ground state in NiO can be described as a mixture of I $3d^8$> and I $3d^9L$> states, where L stands for a hole located at the oxygen site (charge transfer oxide).[45] He suggests that the satellite peak can be attributed to a $c3d^9L$ final state in which the core hole (c) is shielded by an oxygen 2p valence electron, while the satellite is of $c3d^8$ character. This interpretation is consistent with Kim's interpretation of charge transfer transitions from O_{2p} band to Ni_{3d} band accompanying the photoemission process.[47−49] On the other side, Van Veenendaal and Sawatski explain by cluster calculation the presence of a second satellite peak located at about 10.0 eV from the main core level line, which would result from an overlap between an ionized frozen ground state and the unscreened final state of the $3d^8$ character.[50]

These satellite peaks have been taken into account in several recent studies in the literature for the characterization of this type of oxidized compound. It has been shown that the ratio between the core level peaks (the sum of the contributions of the two NiO peaks or the single hydroxide/oxyhydroxide peak) and the intensity of the satellite peaks (hereafter referred to as SR) is specific to each compound and can complete the identification of compounds based on the binding energies of the core level peaks. Values reported in literature[39−41,51−61] and gathered in Table 1 clearly show that NiO, $Ni(OH)_2$, and $NiCo_2O_4$ present SR values between 1.2 and 1.9, while NiO(OH) SR is higher, between 3.0 and 4.0. Consequently, the SR calculation appears as a helpful parameter to identify oxidized compounds of nickel, i.e., to distinguish between oxyhydroxides and hydroxides.

For a complete description of the spectral region at the 2p level where metallic nickel is visible, it is also necessary to take into account the plasmon associated with the Ni^0 metal peak. This plasmon loss structure appears at 6.0 eV higher binding energy than the metallic Ni^0 asymmetric peak and is characterized by a fwhm of approximately 2.5 ± 0.2 eV (Figure 1a). Note that the plasmon peak is associated with collective excitations of the metal valence electron with an intensity set to 9 ± 1% of the Ni^0 peak intensity in the peak fitting process.

As part of this study, nickel oxide, oxyhydroxide, and hydroxide powder analysis enabled the creation of a specific "reference" compounds database. The notion of reference as a pure compound is always a tricky one in surface science since chemical or physical phenomena characteristic of low dimensionality can induce different chemistry for the first atomic planes. For this reason, we refer to "reference" compounds as seen by volume techniques such as X-ray diffraction. The XPS spectra of commercial NiO and home synthesized $Ni(OH)_2$ powders have been analyzed. Spectra (b) and (c) in Figure 1 highlight the Ni_{2p} emission region and the different spectral contributions of the 2p level emission mentioned above. Indeed, two components for nickel oxide Ox_{Ni} (in blue) and one component for nickel oxyhydroxide or hydroxide OH_{Ni} (in orange) are needed to optimize the peak fitting process for both NiO and $Ni(OH)_2$ "reference" samples. The binding energy and the peak width are sensitive to the effect of local charge due to surface defects or chemical heterogeneities, therefore small deviations from the reference values can be observed. Therefore, binding energies and fwhm are allowed to vary over a limited range to account for these effects during peak fitting. It should be noted that the ratio of the intensities of the two oxide components is different for the NiO and $Ni(OH)_2$ samples, revealing a difference in the structure (local order) of the surface of these two compounds. With regard to the satellites, the two peaks located at about 6.0 and 10 eV higher energy than the lowest binding energy NiO

https://doi.org/10.1021/acsomega.4c05082
ACS Omega 2024, 9, 40707−40722

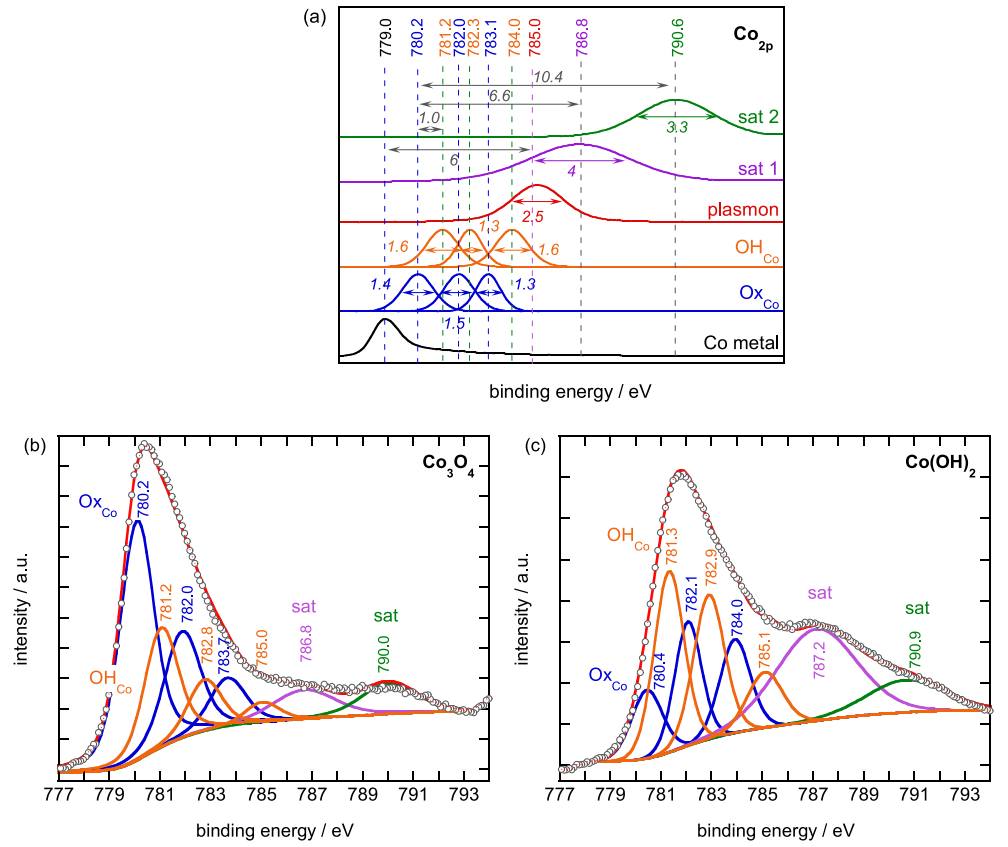

Figure 2. (a) Schematic representation of the different components describing the Co_{2p} spectral fingerprint (extracted values from literature) and experimental spectra of (b) Co_3O_4 and (c) $Co(OH)_2$ included the different spectral contributions.

peak allow a satisfactory fit of the experimental spectra. Looking at the different contributions in Figure 1, the presence of hydroxides on the surface of pure oxide samples as well as some oxides on the surface of pure hydroxides is evident. This is in contrast to the conclusion drawn from the XRD characterization. This is confirmed for each compound by the O_{1s} core-level peak (not shown), which clearly evidences three components located at about 530.0 eV (O^{2-}), 531.4 eV (OH^- or O^{2-} in a defective environment), and 533 eV (H_2O). Finally, this result is not surprising as the chemical structure of the sample is modified between the surface ultimate atomic layers probed by XPS and those in the bulk mainly probed by XRD as mentioned previously. In particular, the hydroxylation of the oxide surface is a natural phenomenon in a humid environment, as is the partial dehydration of the hydroxide surface.

Cobalt Compounds. As reported in several studies mentioned above,[33,37,51,62,63] the photoemission spectrum of the cobalt 2p level is also complicated. Chemical shifts, multiplet structures, and satellite peaks are correlated with the structures of the different compounds. In fact, in the various cobalt compounds considered in this paper, oxide (CoO, Co_3O_4, $NiCo_2O_4$), oxyhydroxide (CoO(OH)), hydroxide ($Co(OH)_2$), and cobalt cations are found in the Co^{2+} and/or Co^{3+} valence states, located in octahedron or tetrahedron sites, depending on the compound crystallography. As with nickel, the site symmetry of the cobalt cations induces a 3d orbital degeneracy of the t_{2g} and e_g levels. Thanks to the works of Biesinger and Grosvenor[38,40] and more recently by Lykhach,[52] who performed a quantitative analysis of the oxidation states of cobalt oxides by resonance photoemission spectroscopy, three main peaks can be attributed to the 2p emission of cobalt cations in the spinel Co_3O_4. The peak with lower binding energy is clearly assigned to Co^{3+} cation, while the two peaks with higher binding energy are assigned to Co^{2+} cation.[52] The single-peak structure of the Co^{3+} cation in the octahedral environment can be attributed to its low spin state ($S = 0$), while the doublet structure of the Co^{2+} cation in the tetrahedral sites could be related to its high spin state ($S = 3/2$). Here again, the intensity ratio of the doublet can be influenced by local disorder (hole screening relaxation or crystal field variation due to local deformation), However, these effects have not been clearly investigated in any studies. On the other hand, the intensity ratio between the Co^{3+} and Co^{2+} peaks, noted $\frac{I^{ox}_{3+}}{I^{ox}_{2+}}$, is well-defined in the case of a nondefective compound. The theoretical value of $\frac{I^{ox}_{3+}}{I^{ox}_{2+}}$ is two for a perfect spinel structure.

As for nickel, two other large contributions (satellite peaks) appear with binding energies of circa ≃6 and ≃10 eV higher than the first core-level peak (787 and 790 eV, respectively). Some studies attribute satellites to a strong hybridization between the localized 3d states and the O_{2p} valence orbitals, similar to that discussed previously for nickel oxides. Kim explains that satellites could be due to the combined effects of monopole charge transfer (O_{2p}-Co_{3d}), multiplet splitting, and the crystal field effect. Charge transfer is dominant over the other effects.[33] Frost's works on various cobalt complexes[62] show that high-spin Co^{2+} compounds have high-intensity satellites, while low-spin Co^{3+} compounds have low intensity

https://doi.org/10.1021/acsomega.4c05082
ACS Omega 2024, 9, 40707−40722

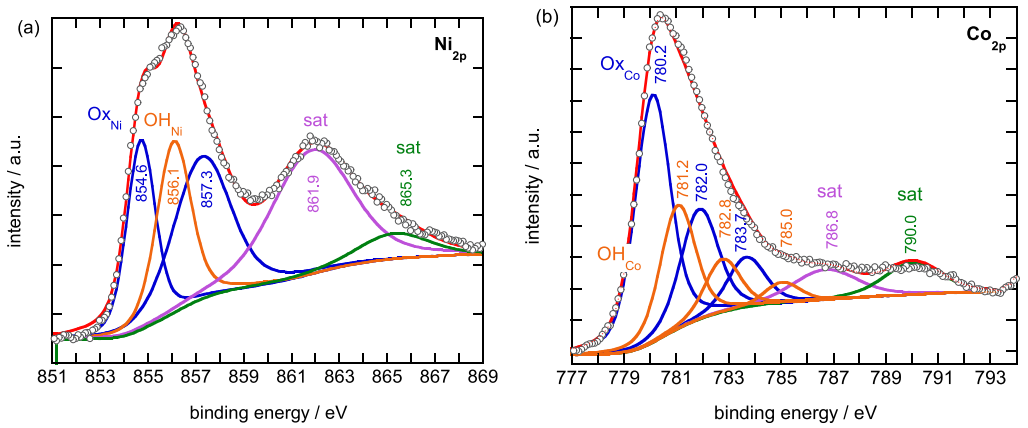

Figure 3. (a) Ni_{2p} and (b) Co_{2p} spectral regions of $NiCo_2O_4$ with the different spectral contributions.

satellites. Frost proposes that satellites are predominantly the result of the shakeup process, without ruling out the possibility of configuration interaction. The origin of satellites as a result of the shakeup process is also supported by Lykhach's work.[52]

Therefore, as for the 2p nickel core level, both the core level binding energy and the satellite intensities can be used to distinguish between cobalt oxide and hydroxide compounds. In this work, considering Co_3O_4, we reasonably reproduce Biesinger and Grosvenor spectrum[38,40] with three peaks located at 780.2 ±0.1, 782.1 ±0.1, and 783.1 ±0.2 eV (Figure 2b). The lowest binding energy satellite is located at ≃787.0 ± 0.2 eV, and the highest binding energy satellite is located at about 790.8 ± 0.2 eV. Nevertheless, it is clear that three more components need to be added in order to satisfactorily complete the experimental spectra that fit over the whole range of binding energies (777−794 eV). These components could be associated with surface hydroxylated compounds OH_{Co} ($Co(OH)_2$ or CoO(OH)), as they are correlated with the presence of an OH peak in the O_{1s} spectrum.[24,27] These three components are located at 781.3 ± 0.1, 782.3 ± 0.1, and 784.0 ± 0.1 eV. It looks like an overall shift toward higher binding energies of the oxide peaks of about 1 eV, which agrees with the observations made by Yang.[41]

The experimental ratio $\frac{I^{ox}_{3^+}}{I^{ox}_{2^+}}$ for Co_3O_4 triplet (Figure 2a) is about 1.4 instead of the expected theoretical value of 2. Hence, the spinel contains defaults, and Co^{2+} is in excess. This can be due to oxygen vacancies (leading to some CoO in Co_3O_4) and/or the replacement of oxygen by hydroxyl groups. Both mechanisms are plausible, and the latter could explain the OH contribution in the O_{1S} spectrum.

The existence of CoO on the Co_3O_4 surface, or Co_3O_4 on the surface of CoO, has been observed by Chuang et al.[63] and Grimblot et al.[64]

Concerning the OH_{Co} oxyhydroxide/hydroxide triplet (Figure 2b), no spectral identification related to cation valency has been found in the literature, as is the case for the oxides. The presence of three peaks could then be attributed to a mixture of $Co(OH)_2$ and CoO(OH) or to compounds with defective sites (Co^{3+} in $Co(OH)_2$ or Co^{2+} in CoO(OH)). We could therefore assume that the lowest binding energy peak is due to Co^{3+} cations, while the two peaks located at higher binding energy correspond to Co^{2+} anions in the hydroxylated compound.

The experimental spectrum of $Co(OH)_2$ can be fitted with the same contributions used to fit the experimental spectrum of Co_3O_4 (Figure 2c): three components related to an hydroxylated compound, three components related to the 2p emission from the Co^{2+} and Co^{3+} cations of the oxide compound, and two satellite peaks at higher binding energy.

The $\frac{I^{ox}_{3^+}}{I^{ox}_{2^+}}$ low value of around 0.35 indicates the presence of a mixture of CoO and Co_3O_4 in the surface layer of $Co(OH)_2$, which increases, by the way, the percentage of Co^{2+}. From Figure 2b,c, "reference" spectra evidence higher satellite intensities for Co^{2+}-rich compound than for Co^{3+}-rich compound, in perfect agreement with previous works.[37,41,63]

It is also interesting to look at the 2p spectra of a compound such as $NiCo_2O_4$, which contains both Co and Ni cations (Figure 3). As described above, the Ni_{2p} XPS spectrum requires two components for the oxide and one for the hydroxide (Figure 3a). Similarly, for cobalt, three components for the oxide and three components for the hydroxide are required to fit the experimental Co_{2p} spectrum (Figure 3b). These results are consistent with previous comments about hydroxylation at the oxide surface. In both Ni_{2p} and Co_{2p} spectra, approximately 30% of the signal is attributed to the hydroxylated surface of the spinel compound. Besides, in the case of the cobalt 2p spectrum, the oxide component shows a $\frac{I^{ox}_{3^+}}{I^{ox}_{2^+}}$ ratio at ca. 1.5, which is the same order of magnitude as that for Co_3O_4 spinel spectrum. A surface defective anionic spinel or the presence of some CoO in the top layer mixed with oxyhydroxides/hydroxides can be assumed.

Method for Determining the Surface Composition of Ni and Co Oxides/Oxyhydroxides/Hydroxides by XPS Using the Peak-On-Satellite Ratio. The spectral characteristics of the various oxidized or hydroxidized cobalt and nickel compounds are determined for a few "reference" compounds. These spectral fingerprints can be used to study the composition of the surface layer of "reference" compounds as well as the passivating layer of the $Co_{20}Ni_{80}$ alloy. Considering the previous section, it is clear that the spectral contributions of Ni/Co oxides, oxyhydroxides, and hydroxides partially overlap but can be distinguished based on (i) a peak fitting of the multiplet structure, (ii) the energy position of their 2p core level photoemission spectra, and (iii) the intensity of the satellite peaks. However, in the case of a thin film consisting of a mixture of several oxidized compounds, determining the contribution of different oxides or oxyhydroxides/hydroxides can be difficult without a rigorous method of spectral deconvolution, especially as the spectrum

https://doi.org/10.1021/acsomega.4c05082
ACS Omega 2024, 9, 40707−40722

of a compound in a mixture can be slightly shifted from the pure reference spectrum.

Therefore, in these complex cases, we propose that the qualitative and quantitative identification of each oxidized species can be carried out using the peak-to-satellite ratio (SR). SR is a parameter that takes into account satellite peak intensity relative to 2p peak intensity. As compound identification using only the 2p levels fingerprint can be a complicated task due to peaks overlaps, the additional information brought by the peak-to-satellite ratio parameter will be more discriminative to identify the different compounds present in the oxidized layer. Both for Ni and Co, each compound i has its own characteristic value of SR_i. As a result, $NiCo_2O_4$ has 2 SR values: one for Co and one for Ni.

Table 1 gathers the SR parameter values found in the literature for cobalt and nickel oxides, oxyhydroxides, and hydroxide compounds. For nickel, Ni^{3+} species (NiO(OH)) have a higher SR value than Ni^{2+} species (oxides or hydroxides). The same trend is observed for the cobalt species: Co^{2+} has lower values (from 1.5 to 2.6) than Co^{3+} (from 5.0−6.5 to 8.0−10.0). In the case of spinel, the SR associated with Ni_{2p} is about 1.9. This value is between the oxide and hydroxide values and the oxyhydroxide value. The SR value associated with Co_{2p} is among the higher ones, ranging from 8.0 to 9.0. Therefore, the experimental SR values complement the core level binding energy positions and fingerprint information to identify the compounds present in the surface layer.

Peak fitting of the Co_{2p} and Ni_{2p} spectra leads to the determination of the intensities of the oxides, hydroxides, and satellites, taking into account the multiplet structures described above. A global SR parameter (SR_{tot}) can then be calculated, which corresponds to the mixture of several oxidized or hydroxylated compounds and can be defined by

$$SR_{tot}^{-1} = \sum_{i=1}^{n} x_i \cdot SR_i^{-1} \quad (1)$$

In eq 1, n stands for the number of chemical compounds, which gives the total 2p spectrum for the mixture (i.e., the number of different oxides, oxyhydroxides, and hydroxides), and SR_i is the SR parameter for a given pure compound i. x_i is the intensity fraction of compound i (oxides, oxyhydroxides, and hydroxides) in the total intensity measured for the mixture, so it results that

$$\sum_{i=1}^{n} x_i = 1 \quad (2)$$

Quantitative determination of cobalt and nickel oxides, oxyhydroxides, and hydroxides compounds then means calculating the different values of x_i from experimental SR_{tot} measurements and characteristic SR_i values found in the literature. A further eq 3 can relate the measured intensities of oxidized (I_{ox}) and hydroxylated (I_{OH}) species to the intensity fractions x_i, requiring the definition of another parameter R_{OxOH}.

$$R_{OxOH} = \frac{\sum_{k=1}^{m} x_k \cdot I_{Oxk}}{\sum_{j=1}^{l} x_j I_{OH_j}} \quad (3)$$

For the Ni_{2p} spectrum, only the three most stable forms of oxidized nickel (NiO, NiO(OH), and $Ni(OH)_2$) were considered. Consequently, eqs 1−3 are sufficient to determine the composition of the mixture. The system of equations is solved using the "solve" function of Mathematica 11 (Wolfram). In order to take into account, the uncertainties of experimental measurements on the various parameters (measured and reference), this "solve" function has been integrated into several loops, allowing a discrete variation (≈10%) of the parameters in intervals centered on the measured and reference values.

In the case of the Co_{2p} spectrum, the system is more complex as four compounds (CoO, Co_3O_4, CoO(OH), and $Co(OH)_2$) can be considered. However, it is possible to determine the composition of the mixture by means of a fourth equation that links the intensity fractions x_i and results from the distinction between the Co^{2+} and Co^{3+} signals in the 2p spectra, as shown above.

Finally, it is more interesting to determine the molar percentage (z_i) of each constituent of the oxidized layer, rather than to look at its intensity fraction (x_i) in the XPS spectra. These two values are not the same because the different oxidized species do not have the same 2p emissivity (not the same atomic density of emitting atoms). Compound percentage z_i in the surface layer can thus be evaluated from the intensity fractions and the atomic density (photoelectron emitters $PED_i = \rho_{ei}$) as follows (eq 4):

$$z_i = \frac{x_i/\rho_{ei}}{\sum_{k=1}^{n} x_k/\rho_{ek}} \times 100 \quad (4)$$

using the ρ_{ei} values reported in literature and listed in Table 2.

Table 2. Crystal Structure, Volume Mass ρ, and Photoelectron Emitter Density ρ_e of Different Co and Ni Compounds

Compound	Crystal structureSpace group	ρ/g cm^{-3}	ρ_e/at nm^{-3}
Co	Hexagonal$P6_3/mmc$	8.9	100
CoO	CubicFm-3m	6.4	51
Co_3O_4	CubicFd-3m	6.1	54
CoO(OH)	TrigonalR-3m	4.3	28
$Co(OH)_2$	TrigonalP-3m1	3.6	23
Ni	CubicFm-3m	8.9	100
NiO	CubicFm-3m	6.7	54
NiO(OH)	TrigonalR-3m	3.2	20
$Ni(OH)_2$	TrigonalP-3m1	4.1	26

Application to Surface Composition of Some Ni and Co Oxides, Oxyhydroxides, or Hydroxides Reference Compounds. First, the method described above was applied to the "reference" cobalt and nickel compounds that have been previously characterized by X-ray diffraction. An estimation of the surface layer thickness where the chemical composition or structure is different from the bulk one can be determined. Finally, the observed results are compared with those found in the literature.

As already discussed, Figures 1 and 2 showed that hydroxides can be present on the surface of pure oxides, and reversely, oxides can be present on the surface of pure hydroxides. From the calculation of the intensity fractions x_i based on the measurement of the SR parameter according to the method presented just above, the molar percentages z_i of the different compounds have been determined (eq 4). By differentiating eqs 1 and 4, we can estimate a mean error on

https://doi.org/10.1021/acsomega.4c05082
ACS Omega 2024, 9, 40707−40722

Table 3. Intensity Fraction (x_i); Molar Percentage (z_i) of Surface Layer Compounds for Some Reference Compounds Studied in This Work

	Surface layer compounds x_i; z_i						
Reference compounds	NiO	NiO(OH)	$Ni(OH)_2$	CoO	Co_3O_4	CoO(OH)	$Co(OH)_2$
NiO	0.86	0.02; 14	0.12; 86	-	-	-	-
$Ni(OH)_2$	0.63; 92	0.02; 8	0.35	-	-	-	-
Co_3O_4	-	-	-	0.29; 82	0.67	0.03; 12	0.01; 6
$Co(OH)_2$	-	-	-	0.12; 28	0.13; 28	0.15; 44	0.60
CoO(OH)	-	-	-	0.24; 58	0.17; 42	0.59	0.0; 0
$NiCo_2O_4$	0.70; 53	0.25; 41	0.05; 6	0.66; 67	0.33; 32	0.005; 0.5	0.005; 0.5

the calculated percentages of about 10%. The different obtained values are reported in Table 3.

In the case of the pure oxides reported in Table 3, NiO and Co_3O_4, hydroxylated species (oxyhydroxides or hydroxides) are systematically detected with a mixture of hydroxide and oxyhydroxide. These surface hydroxylated compounds can result from surface water dissociation on some surface reactive sites. In the case of pure hydroxides, the $Ni(OH)_2$ surface contains 92% pure oxide and 8% oxyhydroxide. For $Co(OH)_2$, 56% of the surface layer is made of pure oxide and 44% of the oxyhydroxide CoO(OH). This is probably due to a dehydration process.

Once the composition of the surface layer has been determined, the thickness of this thin surface layer, whose compounds are different from those in the bulk, can be estimated by means of either or both eqs 5 and 7, as appropriate. In the case of a thin surface film covering a bulk compound, the surface layer thickness (d) can be roughly determined using the formula of a layer-by-layer description for the solid[65] given below (eq 5):

$$\frac{I_{surf}^{X,t}}{I_{bulk}^{X,t}} = \frac{\lambda_{surf}\cdot I_{surf}^{X\circ}}{\lambda_{bulk}\cdot I_{bulk}^{X\circ}} \frac{(1 - e^{-d/\lambda_{surf}})}{e^{-d/\lambda_{surf}}} \quad (5)$$

In this formula, $I_{surf}^{X,t}$ is the sum of the intensities emitted by all detected surface compounds and $I_{bulk}^{X,t}$ is the intensity of the bulk compounds at an abrasion time t (here, $t = 0$ has been considered for calculation). λ_{surf} and λ_{bulk} are the transport mean free paths (inelastic and elastic collisions taken into account) for the surface thin film of thickness d and of the bulk reference compound (bulk oxide or bulk hydroxide) under the surface layer, respectively. λ_{surf} is related to the effective attenuation length. λ_{surf} and λ_{bulk} values are taken from the literature. The usual cosine factor appearing in the attenuation law is set to one because the photoelectrons are collected perpendicular to the sample surface. Much work has been done in the field of electron spectroscopy quantification by authors such as Seah,[66,67] Tanuma et al.,[68,69] or Jablonski[70,71] to calculate or determine the inelastic mean-free path and effective attenuation length (EAL). The recent work of Powell[72] proposes two predictive equations for the determination of the EAL used for measurement of overlayer film thicknesses on a planar substrate as well as on nanostructures by XPS. Following this work, we expect an EAL value near 1.1 ± 0.1 nm for metals at the kinetic energy of the 2p photoelectrons. An EAL close to 1.4 ± 0.1 nm can be used for oxides or hydroxides. Note that the EAL depends on physical parameters related to material volume mass (ρ), chemical composition (average atomic number Z), material porosity, or surface topography. Therefore, some uncertainty must be considered when using a given value to determine coating thickness.

In eq 5, $I_{bulk}^{X\circ}$ and $I_{surf}^{X\circ}$ are the intensities emitted by an atomic layer of the bulk and surface compounds, which are both described by a stack of thin atomic layers of thickness d_0 (layer-by-layer model).[73,74] These photoemission intensities, $I_{bulk}^{X\circ}$ and $I_{surf}^{X\circ}$, depend on physical factors as ionization cross section, angular photoemission angular asymmetry factor, the incident photon flux density, or the number of photoemitting atoms par volume unit, for example. The intensity mathematical expression can be found in some works[66,75] and is given in eq 6:

$$I_{2p}^{X} = n_{2p}^{X}\cdot\sigma_{2p}^{X}\cdot N^{X}\cdot A_{2p}^{X}\cdot\lambda_{2p}^{X}\cdot R_{2p}\cdot\sec(\alpha) \quad (6)$$

where n_{2p}^{X} is the number of electrons in the 2p orbital of the atom X, σ_{2p}^{X} is the 2p shell ionization cross section, N^X is the X atom volumetric density, A_{2p}^{X} is the angular photoemission angular asymmetry factor which depends of the orbital shape, λ_{2p}^{X} is the inelastic mean free path for 2p photoelectrons emitted by atoms X, R_{2p} is a backscattering factor, and α is the angle of incidence of the X-ray beam from the surface normal.

Consequently, considering the emission of the same core level (2p) of the same atom X in the surface layer and in the bulk, the $\frac{I_{surf}^{X\circ}}{I_{bulk}^{X\circ}}$ ratio can be estimated according to eq 6 by the ratio of emitting atoms volumetric densities in the surface layer and in the bulk layer $\frac{N_{surf}^{X\circ}}{N_{bulk}^{X\circ}}$ as all the other factors being equal.

In the case of a thin film covering a substrate (metal or reference compound is the bulk), whose signal is visible in the spectrum (thickness less than 3 times the EAL value), eq 7 can be applied.

$$\frac{I_{bulk}^{X,t=0}}{I_{bulk}^{X,t=\infty}} = e^{-d/\lambda_{surf}} \quad (7)$$

In this formula, $I_{bulk}^{X,t=0}$ and $I_{bulk}^{X,t=\infty}$ stand for the bulk compound intensity, respectively, with (the bulk compound covered with oxidized species) and without (the pure compound recovered after complete abrasion) the oxide layer. Note that $I_{bulk}^{X,t=\infty}$ can be obtained by the asymptotic behavior of $I_{bulk}^{X,t}$ when t tends toward infinity, corresponding to a long sputtering time, i.e., the thin oxide film has been completely removed.

The oxidized surface layer thickness for pure cobalt and nickel, as well as the thickness of the perturbed surface layer of the five reference compounds studied in this work: NiO, $Ni(OH)_2$, Co_3O_4, $Co(OH)_2$, and CoO(OH) have been

https://doi.org/10.1021/acsomega.4c05082
ACS Omega 2024, 9, 40707−40722

estimated according to eq 5. The values reported in Table 4, are all in the range of some tenths of nanometers, except for cobalt metal, which shows a thicker oxidized layer of about 3.0 nm.

Table 4. Crystal Structure and Outer Layer Thickness *d* of Different Co and Ni Compounds

Compound	Crystal structureSpace group	*d* (nm)
Co	Hexagonal$P6_3/mmc$	3.00
CoO	CubicFm-3m	-
Co_3O_4	CubicFd-3m	0.40
CoO(OH)	TrigonalR-3m	0.47
$Co(OH)_2$	TrigonalP-3m1	0.33
Ni	CubicFm-3m	0.35
NiO	CubicFm-3m	0.25
NiO(OH)	TrigonalR-3m	-
$Ni(OH)_2$	TrigonalP-3m1	0.49

We now compare our results on "reference" compounds with the literature studies. Analyzing the Co_{2p} and Ni_{2p} spectra has led to the conclusion that the surface of cobalt and nickel oxides and hydroxides is complex and that several compounds can be found there (Table 3). It should be noted that the presence of oxide on the surface of hydroxides has been repeatedly shown. In particular, the study of Liu on $Ni(OH)_2$ magnetic particles has shown that NiO exists on the particles surface.[76] The opposite can also be observed in the case of a passivation layer on nickel and its alloys. For example, the presence of a layer of $Ni(OH)_2$ on NiO in the passivation layer on nickel was shown by Hoppe and Strehblow using angle-resolved X-ray photoelectron spectroscopy.[77] A more recent study by He concerning the role of cationic vacancies on the surface of $Ni(OH)_2$ shows by DFT calculation that only 3.7% of cationic defects can favor surface reconstruction into NiO(OH).[78] Another study by Singh on NiO nanoparticles using XRD, XAS, SEM, and XPS techniques revealed that the surface of NiO nanoparticles can be transformed with the appearance of a surface mixed nickel oxide−hydroxide phase after electrocatalytic reactions.[79] Concerning cobalt oxides or hydroxide systems, the recent study of Abarca on supported nano $Co(OH)_2$ particles (30 nm)[80] shows that the surface of the $Co(OH)_2$ nanoparticles is easily oxidized to Co_3O_4. In the case of single crystal, Kim has highlighted that CoO is covered with a Co_3O_4 thin film.[33]

The present results on "reference" compounds of nickel and cobalt oxides or hydroxides are therefore consistent with several studies showing the complexity of the chemical (and topological) structure of the surface of cobalt and nickel "reference" oxides or hydroxide compounds. Trusting in the XPS methodology previously developed, we will now apply it to analyze the XPS Co_{2p} and Ni_{2p} emission of the passivation layer of the $Co_{20}Ni_{80}$ alloy.

Characterization of $Co_{20}Ni_{80}$ Alloy Passive Layer. XPS analysis was coupled with low-energy ion profilometry to characterize the passivation layer that spontaneously formed on the surface of the $Co_{20}Ni_{80}$ alloy. At each sputtering step, a survey was conducted, and the Ni_{2p}, Co_{2p}, O_{1s}, and C_{1s} spectral

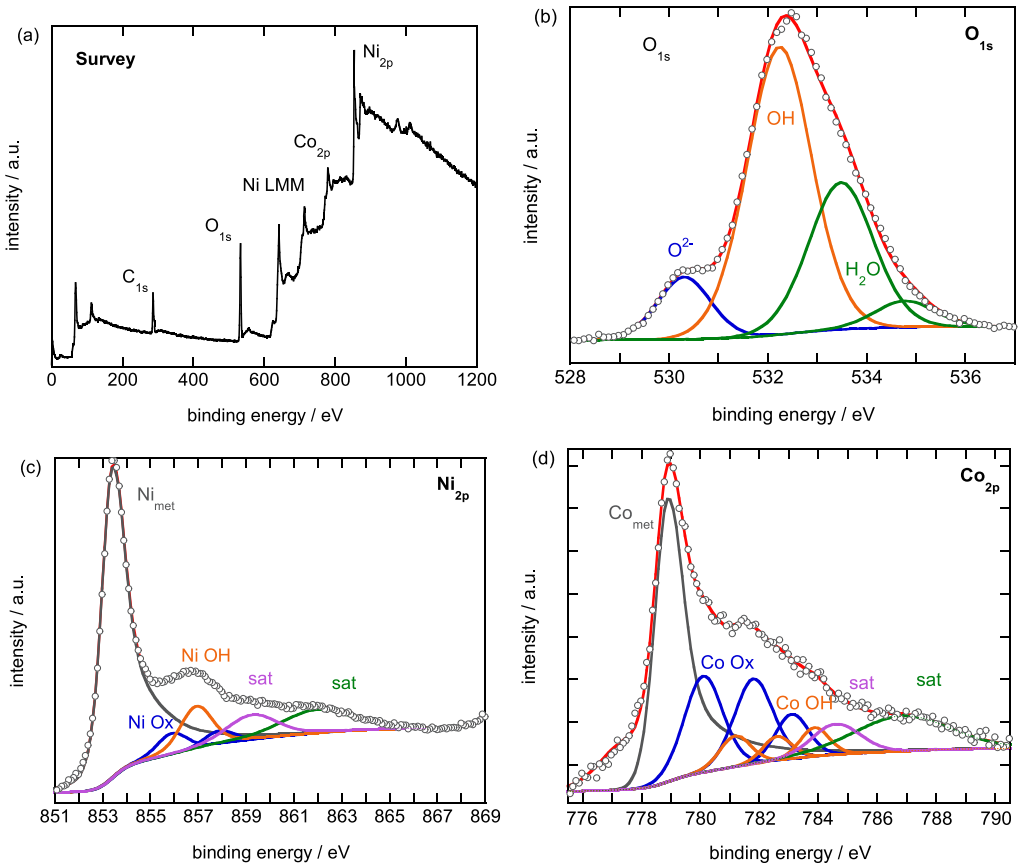

Figure 4. (a) Survey of unsputtered spontaneously oxidized $Co_{20}Ni_{80}$ alloy and XPS (b) O_{1s}, (c) Ni_{2p}, and (d) Co_{2p} spectra with the different spectral contributions.

https://doi.org/10.1021/acsomega.4c05082
ACS Omega 2024, 9, 40707−40722

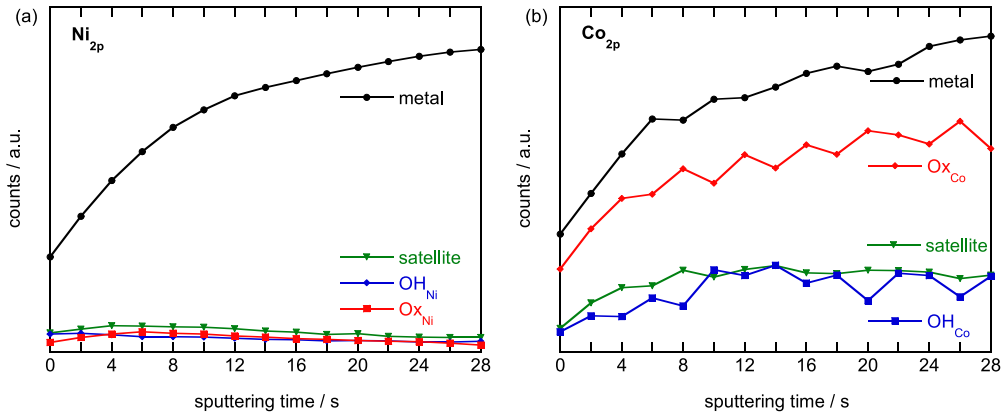

Figure 5. Intensity evolution of metallic component for metal *X*, satellite, OH*X*, and Ox_X peaks for (a) Ni and (b) Co during the depth profile XPS analysis of spontaneously oxidized $Co_{20}Ni_{80}$ alloy.

regions were recorded. Only the 2p level of transition metals has been used, although the 3s spectral region provides interesting information. The O_{1s} spectral region is also of interest since it clearly shows 4 components related to O^{2-} (structural anions of oxides near 531 eV), to OH (hydroxyls by 532.5 eV), and to H_2O (by 533.5 and 534.8 eV). However, the O_{1s} spectral region cannot be used safely because of carbon contamination with oxidized forms of carbon such as C−OH (286−287 eV), C═O (288 eV) or hydrogen carbonates (289−290 eV). Therefore, focusing only on the Ni_{2p} and Co_{2p} spectral regions for quantification avoids any misinterpretation due to oxygen from oxidized carbon contamination. XPS spectra obtained for the $Co_{20}Ni_{80}$ alloy before sputtering are shown in Figure 4.

The survey (Figure 4a) shows the three regions of interest, i.e., Co_{2p}, Ni_{2p}, and O_{1s}. The presence of a C_{1s} peak due to the carbon contamination at about 286−290 eV is clearly visible. The Ni Auger LMM relaxations, consisting mainly of 3 broad bands ($LM_{45}M_{45}$, $LM_{23}M_{45}$, $LM_{23}M_{23}$), with the highest binding energy one appearing to border the Co_{2p} spectral region, are also observed in the 620−820 eV region. The O_{1s} peak (Figure 4b) can be decomposed into 4 contributions, which can be attributed from the lowest to the highest binding energy to O^{2-} anions of the oxide lattice (around 530.2 eV), to hydroxyl ions (hydroxides or OH of organic pollution) (532.3 eV) and to water molecules adsorbed on the surface.

The Ni_{2p} spectral region (Figure 4c) shows an intense Ni^0 peak (metal) at 853.0 eV with an associated plasmon loss at about 6.0 eV toward the highest binding energies (8−10% of the Ni^0 peak area). The peaks of the nickel hydroxides and oxides appear with the same characteristics as those described for the reference samples, i.e., two peaks for the nickel oxides and a peak located between them for the nickel hydroxides.

We can see that the contribution of the hydroxides is more important than that of the oxides. The fact that the area of the metal peak is important compared to that of the oxide, oxyhydroxide, and hydroxide peaks is due to the fact that the passivation layer is relatively thin (much less than 3 times the previously mentioned EAL: 1.1 and 1.4 nm, respectively, for metal and oxidized compounds), corresponding to a weak attenuation of the photoelectrons coming from the underlying metal. The satellite located at 862.5 eV is of high intensity in comparison with the core-level peak intensities of nickel oxide and hydroxide. The resulting SR_{tot} is ca. 1.4. This value is consistent with the presence of NiO and $Ni(OH)_2$ (Table 1).

Concerning the Co_{2p} spectral region, the same comments can be made as for nickel. However, even though the metal peak seems to be important compared to the oxide and hydroxide peaks, the metal/oxide−hydroxide intensity ratio is lower than for nickel. This difference can probably be explained by a difference in the thickness of the cobalt oxyhydroxide passive layer compared to the one containing nickel compounds. This observation suggests that the passivation layer on the $Co_{20}Ni_{80}$ alloy is chemically and topologically inhomogeneous. In the next part of this paper, the heterogeneity in thickness and topology of the thin film will be investigated in a much more quantitative way. Figure 5 shows the evolution of the intensities of the different spectral components of the Ni_{2p} and Co_{2p} regions (metal *X*, oxide (Ox_X), hydroxide/oxyhydroxide (OH_X), satellite) as a function of the ion abrasion time. A first observation concerns the ratio between the intensities of oxide, oxyhydroxide, and hydroxide (I_{OxOH}) and metal (I_{met}) for the two constituting elements of the unsputtered alloy (t = 0 s). Ratio I_{OxOH}/I_{met} values of ≈1 and 0.2 are calculated for the Co_{2p} and for the Ni_{2p}, respectively. This significant difference confirms that the nickel oxide−hydroxide layer is thinner than the cobalt oxide−hydroxide one. This can be explained by the slightly higher affinity of cobalt for oxygen than that of nickel, as has already been pointed out in the case of Co−Ni alloys oxidized at high temperatures.[81] Conversely, the distribution of the oxidized compounds on the surface is very different: at high temperatures, the surface film consists of a (Co, Ni)O solid solution, whereas in the present case, it can be assumed that some parts of the alloy surface are covered with nickel compounds, while others are covered with cobalt compounds. It can also be seen that oxides are more important than hydroxides for cobalt, while the opposite is true for nickel.

The same calculation method as described for the model compounds was then applied to all the spectra recorded during the sputtering process. This made it possible to determine the evolution of the relative percentages of the different possible compounds as a function of ion abrasion time. Though $NiCo_2O_4$ and CoO(OH) SR values are both high and close, the fitting calculation did not give any solution related to the existence of the spinel considering the high percentage of hydroxylated compounds. Consequently, the presence of the $NiCo_2O_4$ spinel was excluded in the present study of the $Ni_{80}Co_{20}$ alloy passivation layer.

https://doi.org/10.1021/acsomega.4c05082
ACS Omega 2024, 9, 40707−40722

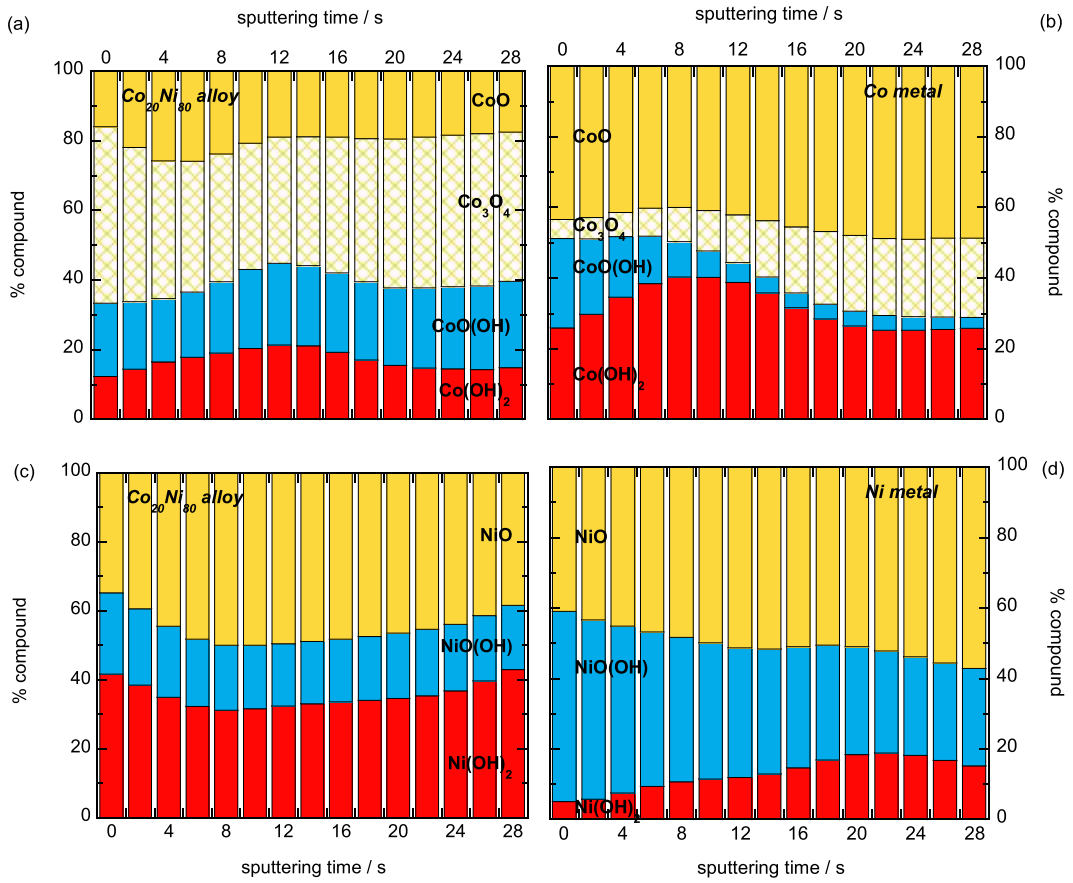

Figure 6. Oxides, oxyhydroxides, and hydroxides relative molar percentages evolution during depth profiling of spontaneous (a), (c) oxidized $Co_{20}Ni_{80}$ alloy, (b) Co metal, and (d) Ni metal.

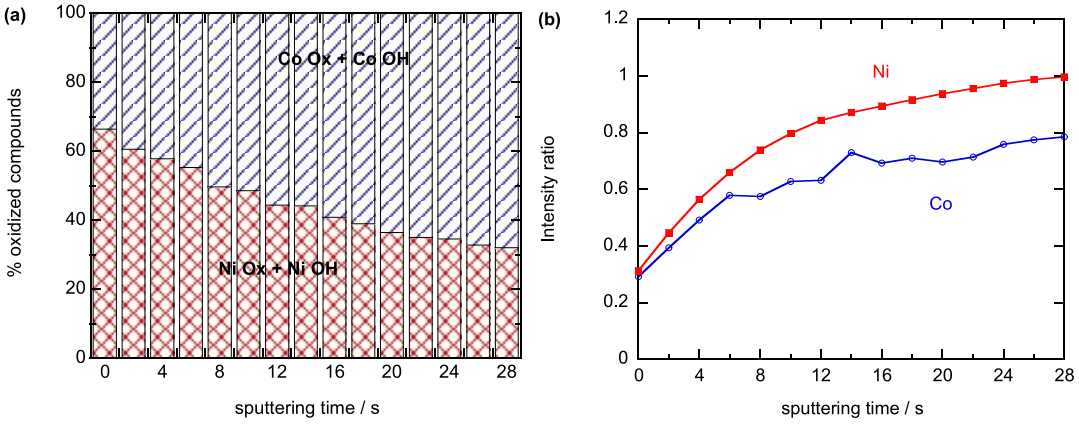

Figure 7. Evolution during depth profiling of (a) the relative percentages of the oxy-hydroxidized compounds of Ni and Co; (b) the infinity ratio (IR) defined in the text for Ni and Co.

The evolution of the composition of the $Co_{20}Ni_{80}$ alloy passive layer is shown in Figure 6a,c, as well as those for pure cobalt (Figure 6b) and pure nickel (Figure 6d).

Figure 6c shows that the dominant nickel compounds on the alloy passivation surface are hydroxides and oxyhydroxides (OHNi ≈ 65%), whereas Figure 6a shows that cobalt oxidized compounds dominate (OxCo ≈ 65%). To get an idea of the relative proportions of compounds of each of the nickel and cobalt elements, the evolution of the relative percentages of oxidized compounds of Ni and Co is shown in Figure 7a. It is clearly shown that nickel compounds dominate over those of cobalt on the outer surface of the passive layer (66−34%) while the reverse is observed with abrasion time (32−68%). In addition, the infinity ratio (IR), i.e., the ratio between the metal peak intensity for the alloy covered by the thin film and that of the clean surface (without any oxide−hydroxide layer), is shown in Figure 7b both for Co and Ni as a function of the abrasion time.

We can observe a different behavior for Ni and Co infinity ratios. IR_{Ni} tends rapidly to 1, while IR_{Co} is still lower than 0.8. This indicates that nickel oxides and oxy-hydroxides are removed from the surface, while cobalt oxides and oxy-

https://doi.org/10.1021/acsomega.4c05082
ACS Omega 2024, 9, 40707−40722

hydroxides are still present. From this observation, it can be argued that some parts of the surface alloy have a pure metallic character, free from oxidized nickel compounds, while others are still covered with oxidized cobalt compounds. This is a strong indication of the heterogeneity of the surface and that the parts of the passivation layer containing the nickel compounds are thinner than the parts containing only the cobalt compounds.

Characterization of $Co_{20}Ni_{80}$ Alloy Passive Layer Thickness and Topology. In the previous section, it was shown that the surface of the $Co_{20}Ni_{80}$ alloy is covered with a mixture of cobalt and nickel oxides, oxyhydroxides, and hydroxides (Figure 6a,c). In addition, the surface layer containing oxidized nickel appears to be thinner than that covered by cobalt compounds (Figure 7b). Therefore, a layer structure where cobalt and nickel species are juxtaposed is considered (Figure 8).

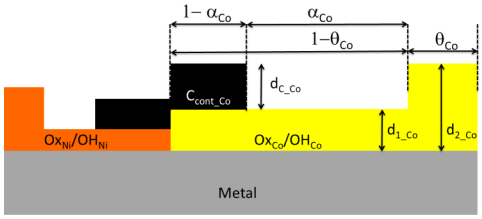

Figure 8. Schematic representation of the model for the passive layer spontaneously formed at the surface of the $Co_{20}Ni_{80}$ alloy.

This part aims to provide a model to elucidate the chemical and spatial structure of the passive layer spontaneously formed on the surface of the $Co_{20}Ni_{80}$ alloy. This model relies on the resolution of a mathematical system that involves eqs 1−3 and 5. Note that, whether for nickel or cobalt, eqs 5 and 7 lead to different layer thicknesses. If the model of a homogeneous surface layer is correct, eqs 5,7 should give the same thickness estimate. This challenges the homogeneous thickness model for both the cobalt and nickel oxide/oxyhydroxide/hydroxide regions. To model the heterogeneity of the oxidized layers, we then propose a simplified spatial distribution, schematized in Figure 8. In this model, for cobalt, for example, a part of the analyzed surface, S_{Co}, is covered with oxidized cobalt compounds. It is made up of zones of different thicknesses (two in the proposed model). This could correspond to the existence of islands covering a θ_{Co} fraction of the S_{Co} surface and of thickness $d_{2_{Co}}$ embedded in a thin film of homogeneous thickness $d_{1_{Co}}$. Carbon contamination is also considered in the thinner part of the layer. This contamination is expected to be of thickness $d_{C_{Co}}$ and cover a $(1 - \alpha_{Co})$ fraction of the thinner layer part. The same description is made for the nickel oxide areas with parameters θ_{Ni}, α_{Ni}, $d_{1_{Ni}}$, $d_{2_{Ni}}$, and $d_{C_{Ni}}$.

A Mathematica code was written for the estimation of the layer structure parameters. It involves equations that link α_X, θ_X, d_{1_X}, d_{2_X}, and d_{C_X} to intensities of the X metal and the oxidized Ox_X and hydroxylated OH_X species by means of eqs 8,9 given below both for Co and Ni that are given in units of an atomic layer emitted intensity. Parameters λ_X (λ_{bulk} in the case of pure metal), λ_{ox} (λ_{surf} in the case of oxidized layer), and λ_C (for carbon contamination) are EAL defined in previous sections and are set, respectively, to 1.1 ± 0.1, 1.4 ± 0.1, and 1.6 ± 0.1 nm. In order to reduce the computation time, we decided to work with the fixed EAL previously cited. The adjustment of the various parameters relating to nickel (α_{Ni}, θ_{Ni}, $d_{1_{Ni}}$, $d_{2_{Ni}}$, $d_{C_{Ni}}$) on the one hand and cobalt on the other hand (α_{Co}, θ_{Co}, $d_{1_{Co}}$, $d_{2_{Co}}$, $d_{C_{Co}}$) is assessed when the calculation results are compatible with the experimental values of $\frac{I_{surf}^{X,t}}{I_{bulk}^{X,t}}$ and $\frac{I_{bulk}^{X,t=0}}{I_{bulk}^{X,t=\infty}}$.

$$I_{surf}^{X,0} = (1-\theta_X)(1-\alpha_X)\lambda_{ox}(1-e^{-d_{1_X}/\lambda_{ox}})e^{-d_{C_X}/\lambda_C} + (1-\theta_X)\alpha_X\lambda_{ox}(1-e^{-d_{1_X}/\lambda_{ox}}) + \theta_X\lambda_{ox}(1-e^{-d_{2_X}/\lambda_{ox}}) \quad (8)$$

$$I_{bulk}^{X,0} = (1-\theta_X)(1-\alpha_X)\lambda_X\, e^{-d_{1_X}/\lambda_{ox}}\, e^{-d_{C_X}/\lambda_C} + (1-\theta_X)\alpha_X\lambda_X\, e^{-d_{1_X}/\lambda_{ox}} + \theta_X\lambda_X(e^{-d_{2_X}/\lambda_{ox}}) \quad (9)$$

In the Mathematica code, α_X, θ_X, d_{1_X}, d_{2_X}, and d_{C_X} are scanned in constrained intervals in nested loops. Parameters value that give and compatible with experimental values are stored and then averaged over all values found by the calculation. Using this model, we found for the thin cobalt oxide−hydroxide film $d_{1_{Co}} = 1.4$ nm and $d_{2_{Co}} = 2.1$ nm, while $d_{1_{Ni}} = 0.9$ nm and $d_{2_{Ni}} = 1.3$ nm for the nickel oxide−hydroxide film. We then confirm that the layers containing cobalt compounds are thicker than those containing nickel compounds. This behavior applies to both the thinnest and the thickest parts of the film. On pure metals, we found $d_{1_{Ni}} = d_{2_{Ni}} = 0.5$ nm for nickel, $d_{1_{Co}} = 2.9$ nm, and $d_{2_{Co}} = 4.9$ nm for cobalt. We can therefore assume that the presence of nickel in the alloy tends to reduce the thickness of the cobalt oxide−hydroxide layers. Conversely, the presence of cobalt in the alloy tends to increase the thickness of the nickel oxide hydroxide layers. It can also be observed that on pure nickel, the oxide−hydroxide layer appears to be homogeneous, with no islands $\left(d_{1_{Ni}} - d_{2_{Ni}}\right)$. Concerning the islands covering, we find approximately 10% of the surface area for both nickel and cobalt parts (respectively, 8 and 11%). Both for Co and Ni oxide layers, we found ca. 35 ± 5% of carbon contamination covering with carbonaceous heaps of thickness of 0.8 ± 0.2 nm. In the case of the $Co_{20}Ni_{80}$ alloy as well as the pure metals, the thin oxide−hydroxide layers appear to consist of a heterogeneous mixture of oxides and hydroxides, both for cobalt and for nickel. On Figure 6b, it can be seen that for pure cobalt, the CoO oxide dominates over Co_3O_4 whereas for the $Co_{20}Ni_{80}$ alloy, it is the other way round (Figure 6a). In terms of hydroxides, more $Co(OH)_2$ than CoO(OH) can be observed on pure cobalt compared to the alloy. Furthermore, the CoO(OH) proportion seems to decrease with sputtering time in the case of pure cobalt. For nickel, it can be seen that NiO(OH) dominates over $Ni(OH)_2$ in the case of the pure metal, in contrast to the $Co_{20}Ni_{80}$ alloy, where the opposite is true.

DISCUSSION

This work, based on the exploitation of the XPS 2p core level of cobalt and nickel, coupled with ion sputtering, highlights that it is possible to identify the chemical compounds present in a thin film spontaneously formed on the surface of either the $Co_{20}Ni_{80}$ alloy, pure Co or Ni metals (Figure 6). A mathematical treatment of the core-level peak-on-satellite

https://doi.org/10.1021/acsomega.4c05082
ACS Omega 2024, 9, 40707−40722

ratio allows the estimation of the geometrical thin film structure as well as the average thickness of the covering thin oxide, oxyhydroxide, or hydroxide films.

The evolution of metallic and oxidized component contributions with sputtering time suggests that the oxidized layer is both chemically and topologically heterogeneous, with areas covered by nickel compounds and others by cobalt compounds, both containing some thicker islands. This type of chemical heterogeneity has already been observed in studies of the structure and composition of passive films on pure metals. In particular, the work of Barr[82,83] shows that CoO, Co_3O_4, CoO(OH), and $Co(OH)_2$ are present on pure cobalt surfaces and contain CoO islands. In the case of pure nickel, this author showed that the oxidized layer is mainly composed of NiO, NiO(OH), and $Ni(OH)_2$, with some Ni_2O_3.

Similar behavior has been observed for various transition element alloys and is well documented in the literature. Co−Cu alloy catalysts exhibit such a distribution.[84] Studies carried out on transition metal alloys like Fe−Cr−Ni by coupling XPS and in situ STM[85,86] also highlight this kind of oxide layer chemical and topological heterogeneity. A bilayer model is proposed for the passivated film: the layer in contact with the metal is made of pure Cr_2O_3 while the outer layer is a mixture of oxides and hydroxides. Besides, the growth of iron and chromium islands at the nanoscale level during in situ oxidation of monocrystalline stainless steel has been demonstrated by STM.[85] Zang's work on Ni−Cr alloys (with Ni as the majority element) passive layers can also be cited.[87] It shows that the passive layer is composed of oxides, oxyhydroxides, or hydroxides and indicates its highly chemically inhomogeneous nature. These works show that at room temperature, pure oxide/oxyhydroxide/hydroxide demixing is more stable than a mixed oxide such as a spinel compound. In this work, in the case of the $Co_{20}Ni_{80}$ alloy, an in-depth distribution evolution can be proposed thanks to the depth profile XPS analysis. Nevertheless, the in-depth chemical heterogeneity should be treated with caution due to the topological lateral heterogeneity. Indeed, an apparent increase in the proportion of a compound with abrasion time can have different explanations: (i) the compound buried in the oxide−hydroxide layer appears more clearly after the overlying compounds have been removed, (ii) compounds present on the surface of thinner parts are removed more rapidly during the abrasion process, resulting in a change in the ratio of compound quantities.

However, in the case of pure nickel metal (Figure 6d), it can be assessed that the compound proportions evolution suggests that NiO is mainly present at the substrate−film interface, while the hydroxylated compounds are rather located at the vacuum−film interface. Hoppe and Strehblow observed the same trend[77] with both NiO(OH) and $Ni(OH)_2$ present near the outer surface. Note that the proportion of nickel hydroxide decreases toward the sample surface and is replaced by oxyhydroxide.

Differences in the oxide layer thicknesses for pure cobalt and pure nickel can be related to metal nobleness. As Kepp points out,[88,89] nobleness is a rather complex concept that relies not only on the standard potential but on various parameters such as 3d band center, electronegativity, relativistic effects, or oxophilicity, for example. Though Co^{2+}/Co standard potential is 0.02 V lower than Ni^{2+}/Ni one, oxophilicity that expresses reactivity with oxygen, is about twice as important for cobalt as for nickel.[89] It could explain the greater oxidizability of the cobalt surface compared with that of nickel, even if other physical parameters are involved in the formation of the oxide layer on the metal (microstructure, metal work function).

This difference in nobleness can be an explanation not only for the difference in oxide layer thickness on pure metals but also for the chemical heterogeneity of the oxide layer on the alloy. Wallwork[90] discusses the cases where competing oxides form on the surfaces of alloys when one of the elements is more noble than the other. He outlines that competition between thermodynamical oxide stability and diffusion kinetics may lead to juxtaposed oxide islands, following Wagner's[91] or Birchenall's[92] models, thus confirming our observations on $Co_{20}Ni_{80}$.

Our study highlights another point: the addition of cobalt to pure nickel to obtain the $Co_{20}Ni_{80}$ alloy slightly modifies the chemical and topological behavior of the passive layer with respect to nickel compounds compared to that obtained in the absence of cobalt. We observe that there is less NiO at the substrate−layer interface than on pure nickel, about 40 vs 60%. This proportion is quite constant throughout the layer present on the alloy surface. By the way, proportions of the three Ni compounds, oxide, oxyhydroxide, and hydroxide, are still quite constant. Note that the proportion of compounds containing the trivalent cation is lower than in the case of pure nickel. It can also be asked whether the presence of cobalt inhibits nickel oxidation to the Ni^{3+} state.

As for pure nickel, hydroxylated species are more concentrated at the vacuum−layer interface and decrease toward the layer−metal interface. Here again, the presence of the other metal, i.e., nickel, seems to influence the layer composition. The in-depth distribution of the different compounds seems much more homogeneous through the film for the $Co_{20}Ni_{80}$ alloy than for the Co metal. Figure 6a clearly shows that the Co_3O_4 oxide proportion compared to the CoO one is strongly increased by the presence of nickel in the alloy. The same trend is observed for CoO(OH) at the expense of $Co(OH)_2$. Considering the comparison of oxides versus hydroxides, the presence of nickel seems to slightly decrease hydroxides at the vacuum−layer interface.

In the case of cobalt oxidation, the opposite behavior to that of nickel is observed. The presence of nickel favors compounds containing trivalent cations (CoO(OH) and Co_3O_4) to the detriment of the divalent compounds ($Co(OH)_2$ and CoO).

Combining these observations with the heterogeneous description of the thin film, it is possible to assert that the oxidation processes of nickel and cobalt in the alloy are modified compared to those observed for each of the pure metals. Indeed, zones containing cobalt have higher levels of CoO(OH), the most oxidized form, than oxidized pure cobalt, while the reverse is true for nickel. It is as if the oxophilicity of cobalt, discussed above, is enhanced in the presence of nickel, an effect comparable to galvanic coupling.

CONCLUSION

The aim of this study was to develop an XPS treatment methodology to characterize the native oxidized film formed spontaneously on the surfaces of nickel, cobalt, and the $Co_{20}Ni_{80}$ alloy, as well as the surface composition of some "reference" cobalt or nickel oxidized compounds. Analysis of 2p core level spectra by peak on satellite ratio (SR), described as a function of that of pure compound SR_i (eq 1), allows the determination of the surface layer composition. For "reference" oxidized nickel and cobalt compounds, we found that the

https://doi.org/10.1021/acsomega.4c05082
ACS Omega 2024, 9, 40707−40722

perturbed zone is of the order of a nanometer, with oxides and oxyhydroxides on hydroxides and vice versa, hydroxides and oxyhydroxides on oxides. At this stage, the results obtained are in line with the literature, which has allowed us to proceed to the final stage of our work, which is the application of the methodology to the $Co_{20}Ni_{80}$ alloy.

In the case of the passive layer on the $Co_{20}Ni_{80}$ alloy, the coupling of the XPS analysis with low energy ion sputtering allows the determination of the in-depth evolution of the chemical compounds in the passive layer. The SR analysis for each time of sputtering has allowed us to confirm the following points: (i) there is no trace of $NiCo_2O_4$ spinel in the oxidized layer; (ii) some parts of the surface are covered with oxidized nickel compounds, while others contain only oxidized cobalt compounds; (iii) whether nickel or cobalt, the oxidized layer is heterogeneous in both composition and thickness. The proposed model consists of islands d_2 distributed in a homogeneous film d_1. This type of heterogeneity has been reported in the literature and may be due, among other things, to the different nobleness of the two elements in the alloy.

Now that the methodology has been fine-tuned, work can begin on a larger scale. The objectives are manifold: to study the influence of the Ni/Co ratio in the alloy on (i) the composition and morphology of the passivation layer and (ii) the corrosion resistance properties. This last point will require XPS analysis to be coupled with electrochemical techniques and may involve coatings that have been oxidized over long periods or under severe service conditions or that have been electrochemically synthesized. Note that this XPS analysis methodology could also be applied to other transition metal alloys containing elements that show satellites in their 2p spectra.

■ ASSOCIATED CONTENT

Data Availability Statement

Raw XPS data in.xls format of $Co_{20}Ni_{80}$ for different abrasion times are available at Zenodo repository at https://doi.org/10.5281/zenodo.13628577.

Supporting Information

The Supporting Information is available free of charge at https://pubs.acs.org/doi/10.1021/acsomega.4c05082.

Containing XRD patterns of synthesized $Co(OH)_2$ (Figure S.I.1), $CoO(OH)$ (Figure S.I.2), Co_3O_4 (Figure S.I.3), $Ni(OH)_2$ (Figure S.I.4), and $NiCo_2O_4$ (Figure S.I.5) (PDF)

■ AUTHOR INFORMATION

Corresponding Author

Barbara Laïk − *University Paris Est Créteil, CNRS, ICMPE, UMR 7182, Thiais 94320, France;* orcid.org/0000-0001-5194-4210; Email: barbara.laik@cnrs.fr

Authors

Morgane Richet − *University Paris Est Créteil, CNRS, ICMPE, UMR 7182, Thiais 94320, France*

Nicolas Emery − *University Paris Est Créteil, CNRS, ICMPE, UMR 7182, Thiais 94320, France;* orcid.org/0000-0003-2724-8789

Stephane Bach − *University Paris Est Créteil, CNRS, ICMPE, UMR 7182, Thiais 94320, France; Département Chimie, Université d'Evry Val d'Essonne, Evry 91025, France*

Loïc Perrière − *University Paris Est Créteil, CNRS, ICMPE, UMR 7182, Thiais 94320, France*

Yvan Cotrebil − *University Paris Est Créteil, CNRS, ICMPE, UMR 7182, Thiais 94320, France*

Vincent Russier − *University Paris Est Créteil, CNRS, ICMPE, UMR 7182, Thiais 94320, France*

Ivan Guillot − *University Paris Est Créteil, CNRS, ICMPE, UMR 7182, Thiais 94320, France*

Pierre Dubot − *University Paris Est Créteil, CNRS, ICMPE, UMR 7182, Thiais 94320, France*

Complete contact information is available at: https://pubs.acs.org/10.1021/acsomega.4c05082

Notes

The authors declare no competing financial interest.

■ ACKNOWLEDGMENTS

This research did not receive any specific grant from funding agencies in the public, commercial, or not-for-profit sectors. The authors thank ICMPE engineers for their technical support (XRD, XPS, metallurgical preparation platform).

■ REFERENCES

(1) Li, Y.; Zhang, X.; Hu, A.; Li, M. Morphological Variation of Electrodeposited Nanostructured Ni-Co Alloy Electrodes and Their Property for Hydrogen Evolution Reaction. *Int. J. Hydrogen Energy* **2018**, *43* (49), 22012−22020.

(2) González-Buch, C.; Herraiz-Cardona, I.; Ortega, E.; García-Antón, J.; Pérez-Herranz, V. Synthesis and Characterization of Macroporous Ni, Co and Ni−Co Electrocatalytic Deposits for Hydrogen Evolution Reaction in Alkaline Media. *Int. J. Hydrogen Energy* **2013**, *38* (25), 10157−10169.

(3) Hong, S. H.; Ahn, S. H.; Choi, I.; Pyo, S. G.; Kim, H.-J.; Jang, J. H.; Kim, S.-K. Fabrication and Evaluation of Nickel Cobalt Alloy Electrocatalysts for Alkaline Water Splitting. *Appl. Surf. Sci.* **2014**, *307*, 146−152.

(4) Duch, M.; Esteve, J.; Gómez, E.; Pérez-Castillejos, R.; Vallés, E. Development and Characterization of Co-Ni Alloys for Microsystems Applications. *J. Electrochem. Soc.* **2002**, *149* (4), C201.

(5) Hernandez-Perez, J. N.; Hernández-Nochebuena, M. A.; González-Scott, J.; González-Huerta, R. D. G.; Reyes-Rodríguez, J. L.; Ortiz, A. Assessment of Data Capture Conditions Effect on Reverse Electrodialysis Process Using a DC Electronic Load. *Energies* **2023**, *16* (21), 7282.

(6) Ma, C.; Wang, S.; Walsh, F. C. The Electrodeposition of Nanocrystalline Cobalt−Nickel−Phosphorus Alloy Coatings: A Review. *Transactions Of The IMF* **2015**, *93* (5), 275−280.

(7) Tsai, S.-Y.; Fung, K.-Z.; Wei, C.-N.; Bor, H.-Y. Thin Film Deposition of Semiconducting Ni-Co Oxide Spinel with Adequate Electrical and Optical Properties for Energy Application. *J. Electron. Mater.* **2014**, *43*, 2584−2587.

(8) Takei, K. T. K.; Maeda, Y. M. Y. NMR Study on Compositional Distribution in Sputter-Deposited Co-Ni Thin Films. *Jpn. J. Appl. Phys.* **1992**, *31* (9R), 2734.

(9) Hsieh, C. T.; Liu, J. Q.; Lue, J. T. Magnetic Force Microscopy Studies of Domain Walls in Nickel and Cobalt Films. *Appl. Surf. Sci.* **2005**, *252* (5), 1899−1909.

(10) Kolb, D. M.; Ullmann, R.; Ziegler, J. C. Electrochemical Nanostructuring. *Electrochim. Acta* **1998**, *43* (19−20), 2751−2760.

(11) Kleinert, M.; Waibel, H.-F.; Engelmann, G. E.; Martin, H.; Kolb, D. M. Co Deposition on Au (111) and Au (100) Electrodes: An in Situ STM Study. *Electrochim. Acta* **2001**, *46* (20−21), 3129−3136.

(12) Pasa, A. A.; Schwarzacher, W. Electrodeposition of Thin Films and Multilayers on Silicon. *Phys. Status Solidi* **1999**, *173* (1), 73−84.

(13) Oskam, G.; Searson, P. C. Electrochemical Nucleation and Growth of Gold on Silicon. *Surf. Sci.* **2000**, *446* (1−2), 103−111.

(14) Ji, C.; Oskam, G.; Searson, P. C. Electrochemical Nucleation and Growth of Copper on Si (1 1 1). *Surf. Sci.* **2001**, *492* (1−2), 115−124.
(15) Kim, K. H.; Lee, J. D.; Lee, J. J.; Ahn, B. Y.; Kim, H. S.; Shin, Y. W. Growth of α-Fe Films on n-Si (111) Substrate by Pulsed Electrodeposition in a Non-Aqueous Solution. *Thin Solid Films* **2005**, *483* (1−2), 74−78.
(16) Manhabosco, T. M.; Englert, G.; Müllle, I. L. Characterization of Cobalt Thin Films Electrodeposited onto Silicon with Two Different Resistivities. *Surf. Coat. Technol.* **2006**, *200* (18−19), 5203−5209.
(17) Messaoudi, Y.; Fenineche, N.; Guittoum, A.; Azizi, A.; Schmerber, G.; Dinia, A. A Study on Electrodeposited Co−Mo Alloys Thin Films. *J. Mater. Sci.: Mater. Electron.* **2013**, *24*, 2962−2969.
(18) Khelladi, M. R.; Mentar, L.; Azizi, A.; Kadirgan, F.; Schmerber, G.; Dinia, A. N. Growth and Properties of Co Nanostructures Electrodeposited on n-Si (1 1 1). *Appl. Surf. Sci.* **2012**, *258* (8), 3907−3912.
(19) Belo, M. D. C.; Hakiki, N. E.; Ferreira, M. G. S. Semiconducting Properties of Passive Films Formed on Nickel−Base Alloys Type Alloy 600: Influence of the Alloying Elements. *Electrochim. Acta* **1999**, *44* (14), 2473−2481.
(20) Hakiki, N. E.; Belo, M. D. C.; Simoes, A. M. P.; Ferreira, M. G. S. Semiconducting Properties of Passive Films Formed on Stainless Steels: Influence of the Alloying Elements. *J. Electrochem. Soc.* **1998**, *145* (11), 3821.
(21) Nakaoka, K.; Ueyama, J.; Ogura, K. Semiconductor and Electrochromic Properties of Electrochemically Deposited Nickel Oxide Films. *J. Electroanal. Chem.* **2004**, *571* (1), 93−99.
(22) Sikora, E.; Macdonald, D. D. Nature of the Passive Film on Nickel. *Electrochim. Acta* **2002**, *48* (1), 69−77.
(23) Darowicki, K.; Krakowiak, S.; Ślepski, P. Selection of Measurement Frequency in Mott−Schottky Analysis of Passive Layer on Nickel. *Electrochim. Acta* **2006**, *51* (11), 2204−2208.
(24) Dorenlor, J. *Contribution à l'étude Du Comportement En Corrosion et Des Évolutions Microstructurales d'alliages Ni-Co: application Au Cas d'un Alliage Ni-20Co Utilisé Dans l'aéronautique*; Normandie Université: Caen, 2021.
(25) TOPAS. *General Profile and Structure Analysis Software for Powder Diffraction*; BRUKER-AXS GmbH: Karlsruhe - Germany, 2022.
(26) Ectors, D.; Goetz-Neunhoeffer, F.; Neubauer, J. A Generalized Geometric Approach to Anisotropic Peak Broadening Due to Domain Morphology. *J. Appl. Crystallogr.* **2015**, *48* (1), 189−194.
(27) Hunt, D.; Garbarino, G.; Rodríguez-Velamazán, J. A.; Ferrari, V.; Jobbagy, M.; Scherlis, D. A. The Magnetic Structure of β-Cobalt Hydroxide and the Effect of Spin-Orientation. *Phys. Chem. Chem. Phys.* **2016**, *18* (44), 30407−30414.
(28) Delaplane, R. G.; Ibers, J. A.; Ferraro, J. R.; Rush, J. J. Diffraction and Spectroscopic Studies of the Cobaltic Acid System HCoC2−DCoO2. *J. Chem. Phys.* **1969**, *50* (5), 1920−1927.
(29) Picard, J. P.; Baud, G.; Besse, J. P.; Chevalier, R. Croissance Cristalline et Étude Structurale de Co3O4. *J. Less Common Metals* **1980**, *75* (1), 99−104.
(30) Kaur, M.; Chand, P.; Anand, H. Effect of Different Synthesis Methods on Morphology and Electrochemical Behavior of Spinel NiCo2O4 Nanostructures as Electrode Material for Energy Storage Application. *Inorg. Chem. Commun.* **2021**, *134*, 108996.
(31) Jugnet, Y.; Duc, T. M. Structure Electronique Des Oxydes de Cobalt CoO et Co3O4. *J. Phys. Chem. Solids* **1979**, *40* (1), 29−37.
(32) Hüfner, S.; Wertheim, G. K. X-Ray Photoelectron Band Structure of Some Transition-Metal Compounds. *Phys. Rev. B* **1973**, *8* (10), 4857.
(33) Kim, K. S. X-Ray-Photoelectron Spectroscopic Studies of the Electronic Structure of CoO. *Phys. Rev. B* **1975**, *11* (6), 2177.
(34) Bagus, P. S.; Ilton, E. S.; Nelin, C. J. The Interpretation of XPS Spectra: Insights into Materials Properties. *Surf. Sci. Rep.* **2013**, *68* (2), 273−304.
(35) Kim, K. S.; Baitinger, W. E.; Amy, J. W.; Winograd, N. ESCA Studies of Metal-Oxygen Surfaces Using Argon and Oxygen Ion-Bombardment. *J. Electron Spectrosc. Relat. Phenom.* **1974**, *5* (1), 351−367.
(36) Kim, K. S.; Winograd, N. X-Ray Photoelectron Spectroscopic Studies of Nickel-Oxygen Surfaces Using Oxygen and Argon Ion-Bombardment. *Surf. Sci.* **1974**, *43* (2), 625−643.
(37) McIntyre, N. S.; Cook, M. G. X-Ray Photoelectron Studies on Some Oxides and Hydroxides of Cobalt, Nickel, and Copper. *Anal. Chem.* **1975**, *47* (13), 2208−2213.
(38) Grosvenor, A. P.; Biesinger, M. C.; Smart, R. S. C.; McIntyre, N. S. New Interpretations of XPS Spectra of Nickel Metal and Oxides. *Surf. Sci.* **2006**, *600* (9), 1771−1779.
(39) Biesinger, M. C.; Payne, B. P.; Lau, L. W. M.; Gerson, A.; Smart, R. S. C. X-ray Photoelectron Spectroscopic Chemical State Quantification of Mixed Nickel Metal, Oxide and Hydroxide Systems. *Surf. Interface Anal.* **2009**, *41* (4), 324−332.
(40) Biesinger, M. C.; Payne, B. P.; Grosvenor, A. P.; Lau, L. W. M.; Gerson, A. R.; Smart, R. S. C. Resolving Surface Chemical States in XPS Analysis of First Row Transition Metals, Oxides and Hydroxides: Cr, Mn, Fe, Co and Ni. *Appl. Surf. Sci.* **2011**, *257* (7), 2717−2730.
(41) Yang, J.; Liu, H.; Martens, W. N.; Frost, R. L. Synthesis and Characterization of Cobalt Hydroxide, Cobalt Oxyhydroxide, and Cobalt Oxide Nanodiscs. *J. Phys. Chem. C* **2010**, *114* (1), 111−119.
(42) Gonzalez-Elipe, A. R.; Holgado, J. P.; Alvarez, R.; Munuera, G. Use of Factor Analysis and XPS to Study Defective Nickel Oxide. *J. Phys. Chem.* **1992**, *96* (7), 3080−3086.
(43) Weidler, N.; Schuch, J.; Knaus, F.; Stenner, P.; Hoch, S.; Maljusch, A.; Schäfer, R.; Kaiser, B.; Jaegermann, W. X-Ray Photoelectron Spectroscopic Investigation of Plasma-Enhanced Chemical Vapor Deposited NiO x, NiO x (OH) y, and CoNiO x (OH) y: Influence of the Chemical Composition on the Catalytic Activity for the Oxygen Evolution Reaction. *J. Phys. Chem. C* **2017**, *121* (12), 6455−6463.
(44) Wertheim, G. K.; Hüfner, S. X-Ray Photoemission Band Structure of Some Transition-Metal Oxides. *Phys. Rev. Lett.* **1972**, *28* (16), 1028.
(45) Tomellini, M. X-Ray Photoelectron Spectra of Defective Nickel Oxide. *J. Chem. Soc., Faraday Trans. 1* **1988**, *84* (10), 3501−3510.
(46) Lobinsky, A. A.; Tolstoy, V. P.; Kodinzev, I. A. Electrocatalytic Properties of γ-NiOOH Nanolayers, Synthesized by Successive Ionic Layer Deposition, during the Oxygen Evolution Reaction upon Water Splitting in the Alkaline Medium. *Nanosyst.: physics., chem., math* **2018**, *9* (5), 669−675.
(47) Kim, K. S.; Davis, R. E. 1-. Electron Spectroscopy of the Nickel-Oxygen System. *J. Electron Spectrosc. Relat. Phenom.* **1972**, *1* (3), 251−258.
(48) Kim, K. S. X-Ray and UV Photoemission Studies of Valence Electronic Structure of NiO. *Chem. Phys. Lett.* **1974**, *26* (2), 234−239.
(49) Kim, K. S. Charge Transfer Transition Accompanying X-Ray Photoionization in Transition-Metal Compounds. *J. Electron Spectrosc. Relat. Phenom.* **1974**, *3* (3), 217−226.
(50) Van Veenendaal, M. A.; Sawatzky, G. A. Nonlocal Screening Effects in 2p X-Ray Photoemission Spectroscopy Core-Level Line Shapes of Transition Metal Compounds. *Phys. Rev. Lett.* **1993**, *70* (16), 2459.
(51) Bonnelle, J. P.; Grimblot, J.; D'huysser, A. Influence de La Polarisation Des Liaisons Sur Les Spectres Esca Des Oxydes de Cobalt. *J. Electron Spectrosc. Relat. Phenom.* **1975**, *7* (2), 151−162.
(52) Lykhach, Y.; Piccinin, S.; Skála, T.; Bertram, M.; Tsud, N.; Brummel, O.; Camellone, M. F.; Beranová, K.; Neitzel, A.; Fabris, S. Quantitative Analysis of the Oxidation State of Cobalt Oxides by Resonant Photoemission Spectroscopy. *J. Phys. Chem. Lett.* **2019**, *10* (20), 6129−6136.
(53) Marco, J. F.; Gancedo, J. R.; Gracia, M.; Gautier, J. L.; Ríos, E. I.; Palmer, H. M.; Greaves, C.; Berry, F. J. Cation Distribution and Magnetic Structure of the Ferrimagnetic Spinel NiCo2O4. *J. Mater. Chem.* **2001**, *11* (12), 3087−3093.

https://doi.org/10.1021/acsomega.4c05082
ACS Omega 2024, 9, 40707−40722

(54) Haenen, J.; Visscher, W.; Barendrecht, E. Characterization of NiCo/Sub 2/O/Sub 4/Electrodes for O/Sub 2/Evolution. Pt. 2. Non-Electrochemical Characterization of NiCo/Sub 2/O/Sub 4/ Electrodes. *J. Electroanal. Chem. Interfacial Electrochem.* **1986**, *208* (2), 297−321.
(55) Umeshbabu, E.; Rao, G. R. NiCo2O4 Hexagonal Nanoplates Anchored on Reduced Graphene Oxide Sheets with Enhanced Electrocatalytic Activity and Stability for Methanol and Water Oxidation. *Electrochim. Acta* **2016**, *213*, 717−729.
(56) Lemoine, A.; Invernizzi, R.; Salvato Vallverdu, G.; Madec, L.; Olchowka, J.; Guerlou-Demourgues, L.; Baraille, I.; Flahaut, D. Surface Reactivity and Surface Characterization of the Layered β (III)-CoOOH Material: An Experimental and Computational Study. *J. Phys. Chem. C* **2021**, *125* (16), 8570−8581.
(57) Mansour, A. N.; Melendres, C. A. Characterization of Ni2O3·6H2O by XPS. *Surf. Sci. Spectra* **1994**, *3* (3), 263−270.
(58) Nk, M. S.; Alex, C.; Jana, R.; Datta, A.; John, N. S. Remarkable CO x Tolerance of Ni 3+ Active Species in a Ni 2 O 3 Catalyst for Sustained Electrochemical Urea Oxidation. *J. Mater. Chem. A Mater.* **2022**, *10* (8), 4209−4221.
(59) Payne, B. P.; Biesinger, M. C.; McIntyre, N. S. The Study of Polycrystalline Nickel Metal Oxidation by Water Vapour. *J. Electron Spectrosc. Relat. Phenom.* **2009**, *175* (1), 55−65.
(60) Mansour, A. N.; Melendres, C. A. Characterization of Electrochemically Prepared γ-NiOOH by XPS. *Surf. Sci. Spectra.* **1994**, *3* (3), 271−278.
(61) Hamdan, M. S.; Othman, M. R. Preparation and Characterization of Nano Size NiOOH by Direct Electrochemical Oxidation of Nickel Plate. *Int. J. Electrochem. Sci.* **2013**, *8* (4), 4747−4760.
(62) Frost, D. C.; McDowell, C. A.; Woolsey, I. S. X-Ray Photoelectron Spectra of Cobalt Compounds. *Mol. Phys.* **1974**, *27* (6), 1473−1489.
(63) Chuang, T. J.; Brundle, C. R.; Rice, D. W. Interpretation of the X-Ray Photoemission Spectra of Cobalt Oxides and Cobalt Oxide Surfaces. *Surf. Sci.* **1976**, *59* (2), 413−429.
(64) Grimblot, J.; d'Huysser, A.; Bonnelle, J. P.; Beaufils, J. P. Application de l'ESCA à l'étude Quantitative de La Réduction de Co3O4. *J. Electron Spectrosc. Relat. Phenom.* **1975**, *6* (1), 71−76.
(65) Seah, M. P. Quantification and Measurement by Auger Electron Spectroscopy and X-Ray Photoelectron Spectroscopy. *Vacuum* **1986**, *36* (7−9), 399−407.
(66) Seah, M. P.; Dench, W. A. Quantitative Electron Spectroscopy of Surfaces: A Standard Data Base for Electron Inelastic Mean Free Paths in Solids. *Surf. Interface Anal.* **1979**, *1* (1), 2−11.
(67) Seah, M. P. An Accurate and Simple Universal Curve for the Energy-dependent Electron Inelastic Mean Free Path. *Surf. Interface Anal.* **2012**, *44* (4), 497−503.
(68) Tanuma, S.; Powell, C. J.; Penn, D. R. Calculations of Electron Inelastic Mean Free Paths. V. Data for 14 Organic Compounds over the 50−2000 EV Range. *Surf. Interface Anal.* **1994**, *21* (3), 165−176.
(69) Tanuma, S.; Powell, C. J.; Penn, D. R. Calculations of Electron Inelastic Mean Free Paths. IX. Data for 41 Elemental Solids over the 50 EV to 30 KeV Range. *Surf. Interface Anal.* **2011**, *43* (3), 689−713.
(70) Powell, C. J.; Jablonski, A. Evaluation of Calculated and Measured Electron Inelastic Mean Free Paths near Solid Surfaces. *J. Phys. Chem. Ref. Data* **1999**, *28* (1), 19−62.
(71) Powell, C. J.; Jablonski, A. Progress in Quantitative Surface Analysis by X-Ray Photoelectron Spectroscopy: Current Status and Perspectives. *J. Electron Spectrosc. Relat. Phenom.* **2010**, *178*, 331−346.
(72) Powell, C. J. Practical Guide for Inelastic Mean Free Paths, Effective Attenuation Lengths, Mean Escape Depths, and Information Depths in x-Ray Photoelectron Spectroscopy. *J. Vac. Sci. Technol., A* **2020**, *38* (2), 023209.
(73) Mitchell, D. F. Quantitative Interpretation of Auger Sputter Profiles of Thin Layers. *Appl. Surface Sci.* **1981**, *9* (1−4), 131−140.
(74) Langeron, J. P.; Minel, L.; Vignes, J. L.; Bouquet, S.; Pellerin, F.; Lorang, G.; Ailloud, P.; Le Hericy, J. An Important Step in Quantitative Auger Analysis: The Use of Peak to Background Ratio. *Surf. Sci.* **1984**, *138* (2−3), 610−628.
(75) Seah, M. P.; Gilmore, I. S.; Spencer, S. J. Quantitative XPS: I. Analysis of X-Ray Photoelectron Intensities from Elemental Data in a Digital Photoelectron Database. *J. Electron Spectrosc. Relat. Phenom.* **2001**, *120* (1−3), 93−111.
(76) Liu, X. H.; Liu, W.; Lv, X. K.; Yang, F.; Wei, X.; Zhang, Z. D.; Sellmyer, D. J. Magnetic Properties of Nickel Hydroxide Nanoparticles. *J. Appl. Phys.* **2010**, *107*, 083919.
(77) Hoppe, H.; Strehblow, H. XPS and UPS Examinations of the Formation of Passive Layers on Ni in 1 M Sodium Hydroxide and 0.5 M Sulphuric Acid. *Surf. Interface Anal.* **1989**, *14* (3), 121−131.
(78) He, Q.; Wan, Y.; Jiang, H.; Pan, Z.; Wu, C.; Wang, M.; Wu, X.; Ye, B.; Ajayan, P. M.; Song, L. Nickel Vacancies Boost Reconstruction in Nickel Hydroxide Electrocatalyst. *ACS Energy Lett.* **2018**, *3* (6), 1373−1380.
(79) Singh, A.; Fekete, M.; Gengenbach, T.; Simonov, A. N.; Hocking, R. K.; Chang, S. L. Y.; Rothmann, M.; Powar, S.; Fu, D.; Hu, Z. Catalytic Activity and Impedance Behavior of Screen-Printed Nickel Oxide as Efficient Water Oxidation Catalysts. *ChemSuschem* **2015**, *8* (24), 4266−4274.
(80) Abarca, G.; Ríos, P. L.; Povea, P.; Cerda-Cavieres, C.; Morales-Verdejo, C.; Arroyo, J. L.; Camarada, M. B. Nanohybrids of Reduced Graphene Oxide and Cobalt Hydroxide (Co (OH) 2| RGO) for the Thermal Decomposition of Ammonium Perchlorate. *RSC Adv.* **2020**, *10* (39), 23165−23172.
(81) Bénard, J.; Bardolle, J.; Bouillon, F.; Cagnet, M.; Moreau, J.; Valensi, G.Les Différents Modes d'oxydation Des Alliages. In *L'Oxydation des Métaux*. Metonorm: Paris; 1962,Vol. *Tome I*. pp. 318340.
(82) Barr, T. L. ESCA Studies of Naturally Passivated Metal Foils. *J. Vac. Sci. Technol.* **1977**, *14* (1), 660−665.
(83) Barr, T. L. An ESCA Study of the Termination of the Passivation of Elemental Metals. *J. Phys. Chem.* **1978**, *82* (16), 1801−1810.
(84) Kupková, K.; Topka, P.; Balabánová, J.; Koštejn, M.; Jirátová, K.; Giraudon, J.-M.; Lamonier, J.-F.; Maixner, J.; Kovanda, F. Cobalt-Copper Oxide Catalysts for VOC Abatement: Effect of Co: Cu Ratio on Performance in Ethanol Oxidation. *Catalysts* **2023**, *13* (1), 107.
(85) Ma, L.; Wiame, F.; Maurice, V.; Marcus, P. Origin of Nanoscale Heterogeneity in the Surface Oxide Film Protecting Stainless Steel against Corrosion. *NPJ. Mater. Degrad.* **2019**, *3* (1), 29.
(86) Ma, L.; Pascalidou, E.-M.; Wiame, F.; Zanna, S.; Maurice, V.; Marcus, P. Passivation Mechanisms and Pre-Oxidation Effects on Model Surfaces of FeCrNi Austenitic Stainless Steel. *Corros. Sci.* **2020**, *167*, 108483.
(87) Zhang, Z.; Ter-Ovanessian, B.; Marcelin, S.; Galipaud, J.; Normand, B. Role of Alloying Elements in Passive and Transpassive Behavior of Ni−Cr-Based Alloys in Borate Buffer Solution. *J. Electrochem. Soc.* **2021**, *168* (8), 081503.
(88) Kepp, K. P. A Quantitative Scale of Oxophilicity and Thiophilicity. *Inorg. Chem.* **2016**, *55* (18), 9461−9470.
(89) Kepp, K. P. Chemical Causes of Metal Nobleness. *ChemPhyschem* **2020**, *21* (5), 360−369.
(90) Wallwork, G. R. The Oxidation of Alloys. *Rep. Prog. Phys.* **1976**, *39* (5), 401.
(91) Wagner, C. Formation of Composite Scales Consisting of Oxides of Different Metals. *J. Electrochem. Soc.* **1956**, *103* (11), 627.
(92) Birchenall, C. E. Oxidation of Metals and Alloys. In *Oxidation of Metals and alloys*, Douglass, D. L., Eds.; Metals Park Cleveland: Ohio, ASM, 1971; p 177.

https://doi.org/10.1021/acsomega.4c05082
ACS Omega 2024, 9, 40707−40722